Topology Optimization of a Coupled Thermal-Fluid System under a Tangential Thermal Gradient Constraint

Xiaoping Qian [*1] and Ercan M. Dede [†2]

[1]Department of Mechanical Engineering, University of Wisconsin-Madison, Madison, WI 53706 - 1572

[2]Electronics Research Department, Toyota Research Institute of North America, 1555 Woodridge Avenue, Ann Arbor, MI 48105

Abstract This paper presents a continuous adjoint approach for topology optimization of a coupled heat transfer and laminar fluid flow system under tangential thermal gradient (TTG) constraints. In this system, the thermal gradient along the boundary of multiple heat sources needs to be controlled. The design goals are to minimize the temperature of the domain, the fluid power dissipation and the TTG along the boundary of the heat sources. The first two goals are combined into a single cost function with weight variables. The TTG is constrained in one of two forms, an integral form where the integral of TTG squares along the boundaries of heat sources is constrained, or a point-wise form where TTG is constrained point-wise. A gradient-based approach is developed to obtain the optimized designs.

A salient feature of our approach is the use of the continuous adjoint approach to derive gradients of both the cost function and two forms of TTG constraints.

Numerical examples demonstrate that the continuous adjoint approach leads to successful topological optimization of the constrained thermal-fluid system. The use of TTG constraint is effective in lowering the TTG along the heat source boundaries. The resulting designs exhibit clear black/white contrast.

Keywords Topology optimization, Thermal fluid system, Continuous adjoint

1 Introduction

Topology optimization is a computational design method for optimally distributing materials in a design domain under governing physics. It originated as a structural optimization

*qian@engr.wisc.edu

†eric.dede@tema.toyota.com

method [1] and has since been applied in problems in fluids, heat transfer, electromagnetic and multiphysics applications [2, 3]. Various methods for topology optimization have been developed. They include density distribution [4, 5, 6], level set [7, 8], topological derivative [9, 10], phase field [11], and evolutionary methods [12].

In the past few years, topology optimization of coupled thermal-fluid systems has been actively explored. For example, Dede used topology optimization to minimize weighted sum of the fluid energy dissipation and the mean temperature of design domain [13] and extended the method to the design of jet impingement target surfaces [14]. The use of topology optimization to design heat dissipating structure under a constant mass flow was studied in [15]. The optimal design of heat sink devices was studied in [16] to maximize heat transfer and to minimize the pressure drop. A constant power input formulation is used to maximize heat transfer in [17]. Topology optimization of the mass flow in a fully coupled natural convection system was recently studied in [18]. A level-set based heat exchange maximization with Tikhonov-based regularization was recently attempted in [19]. In all these studies, finite element methods are used to solve the coupled thermal-fluid equations and discrete adjoints are used to obtain the sensitivity of the objective function with respect to optimization variables. Instead of density-based topology optimization and finite element discretization of Navier-Stokes equations, a combination of a level set method and extended finite element method has been used to solve hydrodynmic Boltzmann equation for topology optimization of scalar transport problems [20]. Finite volume methods have also been used in topology optimization to solve coupled thermal fluid systems. For example, in [21] a bi-objective problem aiming at minimizing the pressure drop while maximizing the recoverable thermal power was attempted where the sensitivity is obtained through discrete adjoint. In [22], a finite volume based continuous adjoint approach to topology optimization of a thermal-fluid system under the Spalart-Allmaras turbulence model was studied, where the design objective is the weighted sum of total pressure losses and temperature rise between inlets and outlet.

An adjoint approach, discrete or continuous, is usually used to obtain sensitivity in topology optimization. A comprehensive review of discrete methods for computing the derivatives of computational models is given in [23]. The continuous adjoint method has been explored in both finite volume based methods for topology optimization, e.g. optimization of duct flow [24] or coupled thermal-fluid systems such as [22], and finite element based topology optimization, e.g. optimization of steady and unsteady incompressible flows [25, 26]. Discussions on the advantages and disadvantages of discrete adjoint and continuous adjoint approaches are available in [27, 28, 29, 30].

This paper presents a continuous adjoint approach for topology optimization of a coupled heat transfer and laminar fluid flow system under tangential thermal gradient (TTG) constraints. The type of problem addressed in this paper differs from most in the literature, as discrete embedded heat sources and thermal gradient constraints are considered. In this system, the thermal gradient along the boundary of multiple heat sources needs to be controlled. The design goals are to minimize the temperature of the domain, the fluid power dissipation and the TTG along the boundary of the heat sources. The first two goals are combined into a single cost function with weight variables. The TTG is constrained in one of the two forms, an integral form where the integral of TTG squares along the boundaries of heat sources is constrained, or a point-wise form where TTG is constrained point-wise. In order to make the point-wise constraints computationally tractable, they are aggregated via the Kreisselmeier-Steinhauser (KS) function into one constraint for topology optimization. A gradient-based approach is developed to obtain the optimized designs. The finite element method is used to solve the coupled thermal-fluid equations with Taylor-Hood elements for the Navier-Stokes equation and linear elements for the heat transfer equation. To avoid checkerboards in the resulting designs, a partial differential equation based density filter [31, 32] is used.

We use the continuous adjoint approach to derive gradients of both the cost function and two forms of TTG constraints. Each function (either a cost function or a constraint) leads to a set of adjoint equations. In each set of adjoint equations, the function is adjoined with the governing state equations, leading to an adjoint heat equation and an adjoint fluid equation. Because adjoint equations are linear with respect to adjoint variables, the cost of solving additional set of adjoint equations is relatively low when compared to the cost of solving non-linear state equations (i.e. Navier-Stokes equations). Our derivation of adjoint systems and gradient expressions is general. It is applicable to any functionals of domain integral, boundary integral or pointwise quantities under thermal-fluid governing equations. We show that the weakly coupled momentum equation in the Navier-Stokes equation and the energy equation for heat transfer lead to weakly coupled adjoint heat transfer equation and adjoint fluid equations.

We use a density-based topology optimization approach [2]. For the flow optimization, a Darcy friction force term is usually added into the Navier-Stokes equations [33]. It can be viewed as a fictitious domain model for viscous flows inside a fluid-porous-solid system governed by Navier-Stokes/Brinkman equations [34]. Such Brinkman penalization has since been frequently used in topology optimization of fluid flow [16, 17, 21, 35, 36]. For the heat transfer, a Solid Isotropic Material Penalization (SIMP) based procedure [4, 5, 6, 2] has been used in [16]. Rational *Approximation of Material Properties (RAMP)* for both Brinkman penalization parameter and thermal conductivity has been used in [37, 21]. In this paper, we use the Brinkman penalization for fluid flow and use a power law to interpolate the thermal conductivity and convection coefficient between the solid phase and the fluid phase. In the interpolation for thermal conductivity, intermediate density is mapped to higher thermal conductivity.

Numerical examples are presented to demonstrate the effects of different weights in the thermal-fluid cost function on the optimized designs. A system energy balance and power analysis provides further quantitative insight into the performance of the designs. The effects and benefits of the two forms of TTG constraints on the optimized designs are also illustrated. The optimized designs exhibit a clear solid-fluid boundary making them suitable for manufacturing.

The remainder of this paper is organized as follows. Section 2 presents the analysis problem and Section 3 presents the optimization problem. The continuous approach to obtaining the adjoint PDEs and gradient expressions is presented in Section 4. The continuous adjoint based optimization approach is briefly presented in Section 5 and numerical results in Section 6. A discussion about the material interpolation for thermal conductivity and specific heat is given in Section 7. This paper concludes in Section 8.

2 The analysis problem

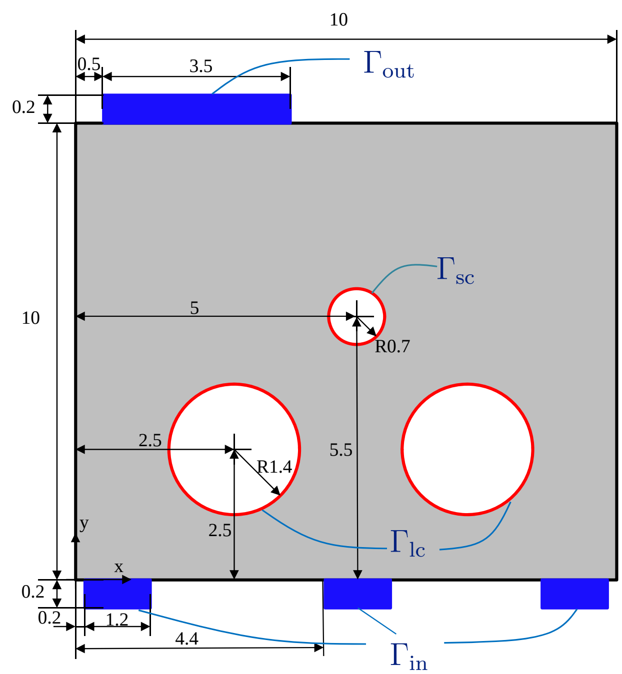

Figure 1: Design specification.

Figure 1 illustrates the dimensional specification of the design problem. The units in the figure are centimetres. The design domain is a square of 10 cm $\times$ 10 cm with three heat generating tubes/cylinders inside. The radius of the smaller tube is 0.7 cm and the radius of the larger tubes is 1.4 cm. The two larger tubes are symmetrically distributed with the center line of the design domain. The left tube is centered at (2.5 cm, 2.5 cm) with respect to the origin of the coordinate system (low-left corner of the design domain). The smaller tube is centered at (5 cm, 5.5 cm). Three inlets are located in the bottom of the design domain. The inlet is of width $L = 1.2$ cm. The outlet at the top is of width 3.5 cm. Each inlet has prescribed velocity $\mathbf{u}_{\Gamma_{\text{in}}} = \dfrac{Re\nu}{L}$ where Re is the Reynolds number and ν is the kinematic viscosity. The outlet has a free flow boundary condition. The inlet boundary Γ_{in}, outlet boundary Γ_{out}, small tube boundary Γ_{sc} and the boundary for large tubes Γ_{lc} are as shown in the figure. The remaining boundary Γ_{rem} is of no-slip condition type. The generated heat flux at the smaller tube is $\bar{q}_{\Gamma_{\text{sc}}}$ at the boundary Γ_{sc} of the small tube and at the boundary Γ_{lc} of the larger tubes is $\bar{q}_{\Gamma_{lc}}$. The inlet temperature is held fixed at 294.15 Kelvin. The remaining boundary is Adiabatic. The design domain is illustrated in grey color. The areas in blue are the fluids in the inlets and the outlet.

The type of problem illustrated in Fig. 1 differs from most in the literature, as discrete embedded heat sources are considered [20]. Specifically, the problem represents a 2-D simplification of a standard benchmark shell and tube heat exchanger [38] found in numerous industry applications. In the context of TTG constraints, the tubes may be considered a heat generating passage, chamber, or cylinder, where the control of the surface temperature is of prime importance from a heat transfer perspective. The design of the surrounding water jackets then becomes a key consideration. A water jacket is a cooling structure commonly used for thermal management of internal combustion engines (ICE)[39] or motors. Temperature at the combustion chamber is linked to engine friction which is then related to overall engine emissions (an important performance criteria). Ideally, we might like to design the combustion process to have a uniform temperature in the circumferential direction of each cylinder with a varying profile in the axial direction since this might impart specific performance advantages. In reality, the flow in a water jacket structure is three dimensional with possible temperature constraints both along the circumference of each combustion chamber as well as the axial direction of each cylinder. There are many interesting design problems that can stem from this topic. However, for simplification in our present study, we focus primarily on a 2-D representation. It should be noted that, beside heat transfer consideration, controlling the surface temperature profile such as temperature uniformity may be beneficial for other applications, e.g. in the reduction of thermal-stress.

2.1 Steady Navier-Stokes equations

The strong form of the boundary value problem for steady flow is stated as follows [40]: find the velocity field $\mathbf{u}$ and the pressure field p, such that

$$-\nabla \cdot \mu(\nabla \mathbf{u} + \nabla \mathbf{u}^T) + \rho(\mathbf{u} \cdot \nabla)\mathbf{u} + \nabla p = \rho \mathbf{b} \qquad \text{in } \Omega \tag{1a}$$

$$\nabla \cdot \mathbf{u} = 0 \qquad \text{in } \Omega \tag{1b}$$

$$\mathbf{u} = \mathbf{u}_{\Gamma_{\text{in}}} \qquad \text{on } \Gamma_{\text{in}} \tag{1c}$$

$$\mathbf{u} = \mathbf{0} \qquad \text{on } \Gamma_{\text{sc}} \cup \Gamma_{\text{lc}} \cup \Gamma_{\text{rem}} \tag{1d}$$

$$\mu \partial_{\mathbf{n}} \mathbf{u} - p\mathbf{n} = 0 \qquad \text{on } \Gamma_{\text{out}} \tag{1e}$$

where $\Gamma_{\text{in}} \cup \Gamma_{\text{out}} \cup \Gamma_{\text{sc}} \cup \Gamma_{\text{lc}} \cup \Gamma_{\text{rem}} = \partial\Omega$ and $\Gamma_{\text{in}} \cap \Gamma_{\text{out}} \cap \Gamma_{\text{sc}} \cap \Gamma_{\text{lc}} \cap \Gamma_{\text{rem}} = \emptyset$, μ is the fluid dynamic viscosity, ρ fluid density, $\mathbf{b}$ the volume force per unit mass of fluid (equal to 0 in this paper) and p denoting the pressure while $\mathbf{n}$ is the outward unit normal. We have Γ_{in} and Γ_{out} as the boundary of the inlets and the outlet, Γ_{lc} and Γ_{sc} are boundaries of the larger tubes and the smaller tube, respectively, and Γ_{rem} represents the remainder of the boundary of the domain. Equation (1a) shows the convection and diffusion of momentum and Equation (1b) shows the flow is incompressible and divergence free. Equation (1e) represents the 'do-nothing' boundary condition and represents a free outflow condition where $\partial_{\mathbf{n}} = \mathbf{n} \cdot \nabla$.

2.2 Conjugate heat transfer model

The domain is under steady-state heat transfer with heat generated from the tubes. The governing equation is

$$
\begin{aligned}
\rho c(\mathbf{u}\cdot\nabla)T &= k_f\nabla^2 T, && \text{in fluid domain} && (2a)\\
0 &= k_s\nabla^2 T + Q, && \text{in solid domain} && (2b)\\
T &= T_0, && \Gamma_{\text{in}} && (2c)\\
-k\mathbf{n}\cdot\frac{\partial T}{\partial \boldsymbol{x}} &= \bar{q}_{sc}, && \Gamma_{\text{sc}} && (2d)\\
-k\mathbf{n}\cdot\frac{\partial T}{\partial \boldsymbol{x}} &= \bar{q}_{lc}, && \Gamma_{\text{lc}} && (2e)\\
-k\mathbf{n}\cdot\frac{\partial T}{\partial \boldsymbol{x}} &= 0, && \Gamma_{\text{out}}\cup\Gamma_{\text{rem}} && (2f)
\end{aligned}
$$

where Q is the heat generation per unit volume, k_s and k_f are, respectively, the thermal conductivity of solid and fluid, ρ is the material density, c specific heat, and $\mathbf{u}$ is the fluid velocity vector. The equation (2) also includes the usual boundary conditions including Dirichlet and Neumann boundary conditions. Equations (2d) and (2e) represent the specified heat flux at the tubes.

Although (2) includes the heat transfer equations for both the fluid domain and the structure domain, the precise separation of the design domain into fluid and solid regions is the goal of the topology optimization.

3 The optimization problem

The goal of our topology optimization problem is to seek an optimal distribution of material density $\gamma(\mathbf{x}), \mathbf{x} \in \Omega$ in the design domain Ω where $\gamma = 1$ represents fluid and $\gamma = 0$ represents solid. We describe below the governing fluid and heat transfer equations for topology optimization, the objective function and the TTG constraints.

3.1 Material interpolations in governing state equations for topology optimization

3.1.1 Governing equations for the Navier Stokes flow

In this paper, we adopt a density-based approach [4, 5, 6, 2] to topology optimization. To incorporate density γ into the governing fluid equation, we follow [33] by introducing a Darcy flow term. Then (1) becomes

$$
\begin{aligned}
-\nabla \cdot \mu(\nabla \mathbf{u} + \nabla \mathbf{u}^T) + \rho(\mathbf{u} \cdot \nabla)\mathbf{u} + \nabla p &= -\alpha(\gamma)\mathbf{u} && \text{in } \Omega && (3a)\\
\nabla \cdot \mathbf{u} &= 0 && \text{in } \Omega && (3b)\\
\mathbf{u} &= \mathbf{u}_{\Gamma_{\text{in}}} && \text{on } \Gamma_{\text{in}} && (3c)\\
\mathbf{u} &= \mathbf{0} && \text{on } \Gamma_{\text{sc}} \cup \Gamma_{\text{lc}} \cup \Gamma_{\text{rem}} && (3d)\\
\mu\partial_{\mathbf{n}}\mathbf{u} - p\mathbf{n} &= 0 && \text{on } \Gamma_{\text{out}} && (3e)
\end{aligned}
$$

where α represents the inverse permeability. The equation is valid for porous media where we assume the fluid flowing in a porous media is subject to a friction force which is proportional to fluid velocity, c.f. Darcy's law.

The inverse permeability between the solid and the fluid regions are interpolated as

$$\alpha(\gamma) = \alpha_{\min} + (\alpha_{\max} - \alpha_{\min})q\frac{1-\gamma}{q+\gamma}, \tag{4}$$

and q serves as the penalty parameter tuning the shape of $\alpha(\gamma)$. The above equation originates from [33] and has been frequently used in topology optimization of fluid flow [16, 17, 21, 35, 36] . It interpolates the following two permeability conditions for the fluid and the solid

$$\alpha_f = \alpha(1) = \alpha_{\min}, \quad \alpha_s = \alpha(0) = \alpha_{\max}.$$

This way, the governing equation in the fluid regions works as if there is no influence from α in the governing equation and in the sold region with zero velocity. In this paper, $\alpha_{\min} = 0, \alpha_{\max} = (1 + 1/Re)/Da$ *[17]* , and $q = 0.1, Da = 1.0e\text{-}4$.

Before we show the weak form of the Navier-Stokes equations, we first define its trial function space and test space. First, the trial solution space $\mathcal{V}$ containing the approximating functions for the velocity is characterized as follows

$$\mathcal{V} = \{\mathbf{u} \in H^1(\Omega) | \mathbf{u} = \mathbf{u}_D \text{ on } \Gamma_D\}.$$

The space of admissible weight (test) functions of the velocity, $\widetilde{\mathbf{u}}$, can be noted as

$$\mathcal{V}_0 = \{\widetilde{\mathbf{u}} \in H^1(\Omega) | \widetilde{\mathbf{u}} = 0 \text{ on } \Gamma_D\}.$$

The space of functions for pressure is denoted as $\mathcal{P}$

$$\mathcal{P} = L_2(\Omega).$$

Note in this paper we use $(\cdot,\cdot)_\Omega$ and $(\cdot,\cdot)_\Gamma$ to refer to the L^2 inner product of two items over the domain Ω and boundary Γ. In this notation, we do not distinguish between scalar-, vector-, tensor- and matrix-valued functions.

By applying integration by parts to (3), we can obtain the weak form of the steady NS equation for topology optimization as follows: find $(\mathbf{u}, p) \in \mathcal{V} \times \mathcal{P}$, such that

$$\mu(\nabla\mathbf{u}+\nabla\mathbf{u}^T, \nabla\widetilde{\mathbf{u}})_\Omega+\rho(\mathbf{u}\cdot\nabla(\mathbf{u}), \widetilde{\mathbf{u}})_\Omega-(\nabla\cdot\widetilde{\mathbf{u}}, p)_\Omega+(\alpha(\gamma)\mathbf{u}, \widetilde{\mathbf{u}})_\Omega-(\nabla\cdot\mathbf{u}, \widetilde{p})_\Omega = 0, \quad \forall(\widetilde{\mathbf{u}}, \widetilde{p}) \in \mathcal{V}_0\times\mathcal{P} \tag{5}$$

where $\widetilde{\mathbf{u}}$ and $\widetilde{p}$ are the test function and the negative sign ahead of $(\nabla\cdot\mathbf{u},\widetilde{p})_\Omega$ is to ensure the symmetry of the problem. The boundary terms after applying the integration by part to the strong form (3) disappear in the above equation. It is because the test function $\widetilde{\mathbf{u}}$ vanishes in the Dirichlet boundary $\Gamma_{\text{in}},\Gamma_{\text{sc}},\Gamma_{\text{lc}}$ and Γ_{rem} and due to the free Neumann boundary condition in (3e) on Γ_{out}. The outflow natural boundary condition leads to vanishing of the boundary terms from the application of Green's formula to the Laplace operator for $\mathbf{u}$ and the gradient of p.

3.1.2 Governing equations for the heat transfer

Through the material interpolation, the heat transfer equations for the fluid (2a) and the solid (2b) domains can be combined as

$$\mathcal{C}(\gamma)\frac{1}{a}(\mathbf{u}\cdot\nabla)T = \nabla\cdot\left(K(\gamma)\nabla T\right), \tag{6}$$

where thermal diffusivity $a=\dfrac{k_f}{\rho c}$ and $K_0 = k_s/k_f$. The material interpolation for relative thermal conductivity and convection are as follows

$$K(\gamma) = (1-\gamma^{p_k})K_0 + \gamma^{p_k}, \tag{7}$$

$$\mathcal{C}(\gamma) = \gamma^{p_\mathcal{C}}, \tag{8}$$

where the power coefficients p_k and $p_\mathcal{C}$ are used to control the non-linearity of the mapping of density to thermal conductivity and convection coefficient. In this paper $p_k = p_\mathcal{C} = 3$ is used throughout all examples unless otherwise noted. It should be noted that this interpolation leads to higher (than linear) thermal conductivity. With the material interpolation, the unified equation (6) represents the fluid when $\gamma = 1$ and the solid when $\gamma = 0$.

Note, if one uses Prandtl number $Pr = \dfrac{\mu}{\rho a} = \dfrac{\nu}{a}$, the above equation becomes

$$\mathcal{C}(\gamma)\frac{Pr}{\nu}(\mathbf{u}\cdot\nabla)T = \nabla\cdot\left(K(\gamma)\nabla T\right). \tag{9}$$

We thus have the following strong form of the heat transfer equation for topology optimization

$$\mathcal{C}(\gamma)\frac{Pr}{\nu}(\mathbf{u}\cdot\nabla)T = \nabla\cdot\left(K(\gamma)\nabla T\right), \qquad \text{in } \Omega \tag{10a}$$

$$T = T_0, \qquad \Gamma_{\text{in}} \tag{10b}$$

$$-k\mathbf{n}\cdot\frac{\partial T}{\partial \boldsymbol{x}} = \bar{q}_{sc}, \qquad \Gamma_{\text{sc}} \tag{10c}$$

$$-k\mathbf{n}\cdot\frac{\partial T}{\partial \boldsymbol{x}} = \bar{q}_{lc}, \qquad \Gamma_{\text{lc}} \tag{10d}$$

$$-k\mathbf{n}\cdot\frac{\partial T}{\partial \boldsymbol{x}} = 0, \qquad \Gamma_{\text{out}}\cup\Gamma_{\text{rem}} \tag{10e}$$

With the following definitions of trial solution space $\mathcal{Q}$ and test space $\mathcal{Q}_0$,

$$\mathcal{Q} = \{T \in H^1(\Omega) | T = \overline{T} \text{ on } \Gamma_T\},$$

$$\mathcal{Q}_0 = \{\widetilde{T} \in H^1(\Omega) | \widetilde{T} = 0 \text{ on } \Gamma_T\},$$

we can define the weak form. The weak form of (10) is: *Find* $T \in \mathcal{Q}$ *such that*

$$\left(K(\gamma)\nabla T, \nabla \widetilde{T}\right)_\Omega + \frac{Pr}{\nu}(\mathcal{C}(\gamma)\mathbf{u} \cdot \nabla T, \widetilde{T})_\Omega + (K(\gamma)\bar{q}, \widetilde{T})_{\Gamma_q} = 0, \quad \forall \widetilde{T} \in \mathcal{Q}_0, \tag{11}$$

where $\Gamma_q = \Gamma_{\text{sc}} \cup \Gamma_{\text{lc}}$.

3.2 Weighted objective function

The objective function has two parts: the heat transfer objective and the fluid power dissipation objective. The heat objective function Φ^h is to minimize the average temperature in the solid region as

$$\Phi^h \equiv (1 - \gamma, T)_\Omega. \tag{12}$$

In this equation, when $\gamma = 1$, the phase is fluid and the term $1 - \gamma$ goes to zero. Thus it represents the average temperature of the solid phase. The objective function for the fluid is to minimize the power dissipation and it can be represented as

$$\Phi^f \equiv \alpha(\gamma)(\mathbf{u}, \mathbf{u})_\Omega + \frac{1}{2}\mu(\nabla\mathbf{u} + \nabla\mathbf{u}^T, \nabla\mathbf{u} + \nabla\mathbf{u}^T)_\Omega. \tag{13}$$

It also reduces to pressure drop between the inlets and the outlet [33]. The heat and fluid objectives can be combined into one objective function via different weights as follows

$$\Phi \equiv w^f \log(\Phi^f + \Delta^f) + w^h \log(\Phi^h + \Delta^h), \tag{14}$$

where w^f and w^h are the weights for the fluid and heat objective, respectively. The use of $\log(\cdot)$ over the fluid and heat objectives is to scale the objective values to facilitate the convergence in numerical optimization. The parameters Δ^f and Δ^h are set to ensure the entries in $\log(\cdot)$ are not too small during optimization. In our numerical implementation, both are set to 100.

3.3 Tangential thermal gradient constraints

We can constrain the tangential thermal gradient (TTG) along the boundary via the following integral form as

$$\Psi^I \equiv (\mathbf{t} \cdot \nabla T, \mathbf{t} \cdot \nabla T)_{\Gamma_{\text{sc}} \cup \Gamma_{\text{lc}}} \leq \theta^I \Psi_0^I, \tag{15}$$

where $\mathbf{t}$ is the tangent along the boundary and $\mathbf{t} \cdot \nabla T$ gives us the TTG. $\theta^I \Psi_0^I$ is some allowed threshold and Ψ_0^I is an initial integral of squared TTG and θ^I is the allowed integral TTG

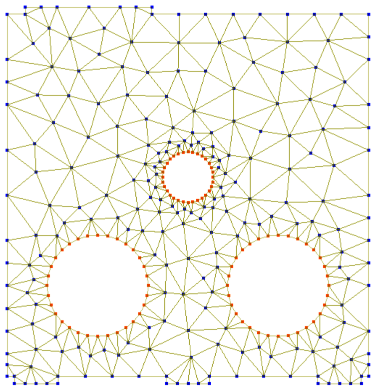

(a) Boundary nodes of the tubes

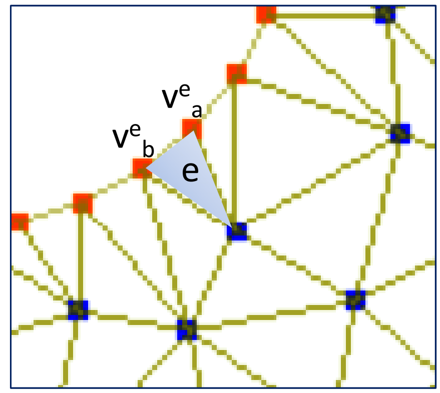

(b) Nodes for computing g_e

Figure 2: Boundary nodes for computing TTG along the boundary.

ratio. We integrate TTG squares over the boundaries of the small circular tube and the two large circular tubes since $\mathbf{t} \cdot \nabla T$ can be either positive or negative.

The integral form of the TTG constraint controlls the overall TTG globally (or in the average sense), but may lead to large TTG locally. An alternative to overcome such potentially high local TTG is to ensure the maximum TTG along the boundary is smaller than a threshold. That is, we can develop a pointwise constraint as

$$(\mathbf{t} \cdot \nabla T, \mathbf{t} \cdot \nabla T)_{\mathbf{x}} \leq \theta^P \Psi_0^P, \quad \mathbf{x} \in \Gamma_{\mathrm{sc}} \cup \Gamma_{\mathrm{lc}}, \tag{16}$$

where $\theta^P \Psi_0^P$ is some allowed threshold, and Ψ_0^P is the initial maximum pointwise squared TTG along the boundaries and θ^P is the allowed pointwise TTG ratio. Since such a pointwise TTG constraint is difficult to implement in numerical optimization, we adopt a discretized form of the point-wise TTG constraint. We assume the design is discretized so that the tube boundaries contain n_{e^b} elements. The TTG of each element g_e should be smaller than a threshold g_0 as

$$(g_e) \leq g_0, \quad e = 1, ...n_{e^b},$$

where g_e represents the square of TTG at the edge of boundary element e and n_{e^b} represents the number of boundary elements, and g_0 is some allowed squared TTG threshold on each point. Because this would lead to a substantial number (n_{e^b}) of TTG constraints, we then propose to aggregate multiple TTG constraints into one constraint through the Kreisselmeier-Steinhauser (K-S) function.

As shown in a coarse linear triangular discretization of the design domain in Fig. 2, we have TTG for element e as $\nabla_t T_e = \dfrac{T_b^e - T_a^e}{L_{ab}}$ where T_a^e and T_b^e represent the temperature at node a and b of element e, respectively, and $L_{ab} = ||\mathbf{v}_a^e - \mathbf{v}_b^e||_2$ represents the length between the node a and b and $\mathbf{v}_a^e$ *and* $\mathbf{v}_b^e$ are their vertex coordinates. The squared TTG of an element can be computed as follows,

$$g_e \equiv \frac{(T_b^e - T_a^e)^2}{L_{ab}^2}. \tag{17}$$

We can use the KS function below to aggregate multiple element-based constraints into one composite function

$$\Psi^P(T) \equiv \frac{1}{\varepsilon} \log \left[\sum_e \exp(\varepsilon g_e) \right] \leq \theta^P \Psi_0^P \tag{18}$$

where Ψ^P is an upper bound of all g_e and ε controls the level of approximation during the aggregation.

Note, we are using linear triangular elements for heat transfer analysis. Therefore, pointwise TTG is the same as element-wise TTG in each element. The aggregated constraint is a function of nodal temperatures where the nodes are boundary nodes along the tubes.

3.4 The optimization problem

With the above defined objective function, the two forms of TTG constraints, and weak form of state equations, we have the following optimization problem.

$$\min_{\gamma} \quad \Phi = w^f \log(\Phi^f + \Delta^f) + w^h \log(\Phi^h + \Delta^h) \tag{19a}$$

$$\text{s.t.} \quad \mu(\nabla \mathbf{u} + \nabla \mathbf{u}^T, \nabla \widetilde{\mathbf{u}})_\Omega + \rho(\mathbf{u} \cdot \nabla(\mathbf{u}), \widetilde{\mathbf{u}})_\Omega - (\nabla \cdot \widetilde{\mathbf{u}}, p)_\Omega \tag{19b}$$

$$+ (\alpha(\gamma)\mathbf{u}, \widetilde{\mathbf{u}})_\Omega - (\nabla \cdot \mathbf{u}, \widetilde{p})_\Omega = 0, \qquad \forall (\widetilde{\mathbf{u}}, \widetilde{p}) \in \mathcal{V}_0 \times \mathcal{P}$$

$$\Big(K(\gamma)\nabla T, \nabla \widetilde{T}\Big)_\Omega + \frac{Pr}{\nu}(\mathcal{C}(\gamma)\mathbf{u} \cdot \nabla T, \widetilde{T})_\Omega + (K(\gamma)\bar{q}, \widetilde{T})_{\Gamma_q} = 0, \quad \forall \widetilde{T} \in \mathcal{Q}_0. \tag{19c}$$

$$(15) \text{ or} (18) \tag{19d}$$

$$V(\gamma)/V_0 \leq \theta^V \tag{19e}$$

where θ^V is the volume fraction of the allowed fluid material over the entire design domain. (19)(a) represents the cost function defined from a weighted combination of the fluid objective Φ^f and the heat objective Φ^h. (19)(b) and (c), respectively, represent the weak form of the Navier-Stokes equations and the thermal equation. (19)(d) refers to the TTG constraint, either the integral form (15) or the pointwise form (18). (19)(e) represents the volume fraction constraint of the design (the density field) γ.

4 Adjoint systems and gradients from the Lagrangian approach

In order to obtain the gradient of the cost function and the TTG constraints with respect to design γ, we use the formal Lagrangian approach [41] to obtain the adjoint systems and the gradient expressions.

We first present a general form of using Lagrangian approach to obtain the adjoint system and the gradient. We then extend the general form to our coupled thermal-fluid state equations.

4.1 First-order optimality condition for general PDE-based optimal design

We give below a general description of the first-order optimality condition for PDE-constrained optimization and show how to obtain the gradient representation through an adjoint system. It should be pointed out that the derivation in this paper follows the formal Lagrangian approach [41]. For rigorous mathematical investigations, readers are referred to [41, 42, 30]. For tutorial introduction on deriving the optimality condition, see [43, 44] .

The general form of a PDE-constrained optimization problem can be stated as follows. Let $\mathcal{U}, \mathcal{A}$ be Hilbert spaces. Our goal is to minimize a functional $\mathcal{J}(u, a) : \mathcal{U} \times \mathcal{A} \to \mathbb{R}$ under the PDE constraint

$$e(u, a) = 0, \quad e : \mathcal{U} \times \mathcal{A} \to Z,$$

where $u \in \mathcal{U}$ represents the state and $a \in \mathcal{A}$ represents a design. We introduce a Lagrange functional $\mathcal{L}$ for the functional $\mathcal{J}$ associated with the constraint $e(u, a)$ as

$$\mathcal{L} : \mathcal{U} \times \mathcal{A} \times \mathcal{Z}^* \to \mathbb{R}, \qquad \mathcal{L}(u, a, v) \equiv \mathcal{J}(u, a) + < v, e(u, a) >_{Z^*, Z}, \tag{20}$$

where v is the Lagrange multiplier (adjoint variable) and Z^*, Z represents the duality pairing. We thus have the following first order optimality condition

$$\begin{aligned}
\mathcal{L}'_u(u, a, v; \widetilde{u}) &= \mathcal{J}'_u(u, a, v; \widetilde{u}) + < v, e'_u(u, a, v; \widetilde{u}) >_{Z^*, Z} = 0 \quad \forall \widetilde{u} \in \mathcal{U} && \text{(21a)} \\
\mathcal{L}'_a(u, a, v; \widetilde{a}) &= \mathcal{J}'_a(u, a, v; \widetilde{a}) + < v, e'_a(u, a, v; \widetilde{a}) >_{Z^*, Z} = 0 \quad \forall \widetilde{a} \in \mathcal{A} && \text{(21b)} \\
\mathcal{L}'_v(u, a, v; \widetilde{v}) &= \qquad < \widetilde{v}, e(u, a) >_{Z^*, Z} = 0 \quad \forall \widetilde{v} \in \mathcal{Z}^* && \text{(21c)}
\end{aligned}$$

where the notation $\mathcal{L}'_u(u, a, v; \widetilde{u})$ denotes the direction derivative of $\mathcal{L}$ with respect to u along $\widetilde{u}$. The first equation in (21) is the so-called adjoint equation and it represents the Lagrangian's variation with respect to the state variable u. The second equation describes the relationship between the adjoint variable v and design a, and the third one is just the state equation.

The optimality condition (21) suggests that, at an optimal design, variations of the Lagrangian functional with respect to all variables must vanish. If (21) is solved directly, it leads to the so-called *one-shot* approach. In this paper, we use a gradient based iterative approach. After solutions of the state equation (21c) and the adjoint equation (21a), $\mathcal{L}'_a(u, a, v; \widetilde{a}) = \mathcal{J}'_a(u, a, v; \widetilde{a}) + < v, e'_a(u, a, v; \widetilde{a}) >_{Z^*, Z}$ in (21b) gives us the gradient and can be used in an iterative optimization approach.

4.2 General optimality conditions under the coupled thermal and fluid PDE constraints

Denote $\mathcal{J}(\mathbf{u}, p, T, \gamma)$ as a functional that can be either the cost functional Φ (14) or the integral form of TTG Ψ^I (15) or point-wise TTG Ψ^P (18), we have the Lagrange functional $\mathcal{L}$ adjoining the functional $\mathcal{J}$ and the governing Navier-Stokes and heat transfer equations as follows

$$
\begin{aligned}
\mathcal{L} \ &= \mathcal{J}(\mathbf{u}, p, T, \gamma) \\
&+\mu(\nabla \mathbf{u} + \nabla \mathbf{u}^T, \nabla \mathbf{v})_\Omega + \rho(\mathbf{u} \cdot \nabla(\mathbf{u}), \mathbf{v})_\Omega - (\nabla \cdot \mathbf{v}, p)_\Omega + (\alpha(\gamma)\mathbf{u}, \mathbf{v})_\Omega - (\nabla \cdot \mathbf{u}, q)_\Omega \\
&+ (K(\gamma)\nabla T, \nabla S)_\Omega + \frac{Pr}{\nu}(\mathcal{C}(\gamma)\mathbf{u} \cdot \nabla T, S)_\Omega + (K(\gamma)\bar{q}, S)_{\Gamma_q},
\end{aligned}
\tag{22}
$$

where $(\mathbf{v} \times q) \in \mathcal{V}_0 \times \mathcal{P}$ are the adjoint variable (Lagrange multiplier) for the fluid state equation (5) and $S \in \mathcal{Q}_0$ is the adjoint variable (Lagrange multiplier) for the heat state equation (11). The Lagrangian's directional derivatives with respect to adjoint variables leads to the primal state equations, i.e. Navier-Stokes equation (5) and heat transfer equation (11).

The adjoint equations are obtained from setting the directional derivatives with regard to state variables $\mathbf{u}, p, T$ in directions $\widetilde{\mathbf{u}}, \widetilde{p}, \widetilde{T}$ as zero. We thus have the following adjoint equations: find $(\mathbf{v}, q) \in (\mathcal{V}_0, \mathcal{P})$ such that

$$
\left.
\begin{aligned}
&\mathcal{J}'_{\mathbf{u}}(\mathbf{u}, p, T, \gamma; \widetilde{\mathbf{u}}) + \mathcal{J}'_p(\mathbf{u}, p, T, \gamma; \widetilde{p}) \\
&\quad +\mu(\nabla \widetilde{\mathbf{u}} + \nabla \widetilde{\mathbf{u}}^T, \nabla \mathbf{v})_\Omega + \rho(\widetilde{\mathbf{u}} \cdot \nabla \mathbf{u} + \mathbf{u} \cdot \nabla \widetilde{\mathbf{u}}, \mathbf{v})_\Omega \\
&\quad +(\alpha(\gamma)\widetilde{\mathbf{u}}, \mathbf{v})_\Omega - (\nabla \cdot \widetilde{\mathbf{u}}, q)_\Omega - (\nabla \cdot \mathbf{v}, \widetilde{p})_\Omega \\
&\quad +\frac{Pr}{\nu}(\mathcal{C}(\gamma)\widetilde{\mathbf{u}} \cdot \nabla T, S)_\Omega
\end{aligned}
\right\} = 0, \quad \forall (\widetilde{\mathbf{u}}, \widetilde{p}) \in (\mathcal{V}_0, \mathcal{P}),
\tag{23}
$$

and find $S \in Q_0$ such that

$$
\mathcal{J}'_T(\mathbf{u}, p, T; \widetilde{T}) + \Big(K(\gamma)\nabla \widetilde{T}, \nabla S\Big)_\Omega + \frac{Pr}{\nu}(\mathcal{C}(\gamma)\mathbf{u} \cdot \nabla \widetilde{T}, S)_\Omega = 0, \qquad \forall \widetilde{T} \in Q_0.
\tag{24}
$$

The above two equations corresponds to the weak form of the adjoint fluid equation and the adjoint heat transfer equation. Comparing (23) and (24), it is clear that the adjoint temperature S appears in the adjoint fluid equations (23). On the other hand, the adjoint fluid variables $\mathbf{v}$ and q do not appear in the adjoint heat equation (24). Therefore, we have the following remark.

Remark 1 When the thermal-fluid system is weakly coupled, its adjoint system is also weakly coupled. The adjoint heat equation can be solved first to obtain S. With the solved S, the adjoint fluid equation is then solved to obtain $\mathbf{v}$ and q.

This suggests that the solution sequence for the adjoint system is reversed from that for the primal system where the Navier-Stokes equations are solved first to obtain velocity $\mathbf{u}$ and then use it to solve the heat transfer equation. Because the adjoint system is weakly coupled, the adjoint heat equations and adjoint fluid equations can therefore be solved sequentially and separately, instead of in a monolithic manner or a staggered fashion as in a strongly coupled system. Similar observation has been reported with the discrete adjoint approach [35].

The gradient representation can be obtained from the Lagrangian's directional derivative with respect to design functional γ and it leads to

$$\begin{aligned}\mathcal{L}'_\gamma(\mathbf{u},p,T,\gamma;\widetilde{\gamma}) = \;& \mathcal{J}'_\gamma(\mathbf{u},p,T,\gamma;\widetilde{\gamma}) \\ & +(\alpha'_\gamma(\gamma)\mathbf{u},\mathbf{v}\widetilde{\gamma})_\Omega \\ & +\left(K'_\gamma(\gamma)\nabla T,\nabla S\widetilde{\gamma}\right)_\Omega + \frac{Pr}{\nu}(\mathcal{C}'_\gamma(\gamma)\mathbf{u}\cdot\nabla T, S\widetilde{\gamma})_\Omega + (K'_\gamma(\gamma)\bar{q}, S\widetilde{\gamma})_{\Gamma_q}\end{aligned} \tag{25}$$

where $\widetilde{\gamma}$ represents the variation of γ. The gradient expression has three components, consisting of the gradients of the cost function, of the weak form of the Navier-Stokes equation, and of the weak form of the heat transfer equation.

It should be noted that the boundary term due to heat flux $\bar{q}$ does not appear in the adjoint system. It only appears in the weak form of the primal heat transfer equation and the gradient expression of $\mathcal{L}(\mathbf{u},p,T,\gamma)$ with respect to design γ.

4.3 Specific forms of adjoint systems

Equations (23), (24) and (25) represent the adjoint system and gradient expression that are applicable to any functional $\mathcal{J}$ under the coupled thermal fluid constraint. These equations can be customized to specific forms of the adjoint equations and gradient expressions for the cost functional and TTG constraints.

For the cost functional Φ (14), we have the following directional derivatives with respect to state variable $\mathbf{u}, p$, and T

$$\Phi'_{\mathbf{u}}(\mathbf{u},p,T,\gamma;\widetilde{\mathbf{u}}) = w^f\frac{1}{\Phi^f+\Delta^f}\left(2\alpha(\gamma)(\mathbf{u},\widetilde{\mathbf{u}})_\Omega + \mu(\nabla\mathbf{u}+\nabla\mathbf{u}^T,\nabla\widetilde{\mathbf{u}}+\nabla\widetilde{\mathbf{u}}^T)_\Omega\right), \tag{26a}$$

$$\Phi'_p(\mathbf{u},p,T,\gamma;\widetilde{p}) = 0, \tag{26b}$$

$$\Phi'_T(\mathbf{u},p,T,\gamma;\widetilde{T}) = w^h\frac{1}{\Phi^h+\Delta^h}(1-\gamma,\widetilde{T})_\Omega. \tag{26c}$$

Plugging the above equations into (23) and (24), we have the following adjoint fluid equation and adjoint heat transfer equation for the cost functional Φ: find $(\mathbf{v}_\Phi, q_\Phi) \in (\mathcal{V}_0,\mathcal{P})$ such that

$$\left.\begin{aligned} & w^f\frac{1}{\Phi^f+\Delta^f}\left(2\alpha(\gamma)(\mathbf{u},\widetilde{\mathbf{T}})_\Omega + \mu(\nabla\mathbf{u}+\nabla\mathbf{u}^T,\nabla\widetilde{\mathbf{T}}+\nabla\widetilde{\mathbf{T}}^T)_\Omega\right) \\ & +\mu(\nabla\widetilde{\mathbf{u}}+\nabla\widetilde{\mathbf{u}}^T,\nabla\mathbf{v}_\Phi)_\Omega + \rho(\widetilde{\mathbf{u}}\cdot\nabla\mathbf{u}+\mathbf{u}\cdot\nabla\widetilde{\mathbf{u}},\mathbf{v}_\Phi)_\Omega \\ & +(\alpha(\gamma)\widetilde{\mathbf{u}},\mathbf{v}_\Phi)_\Omega - (\nabla\cdot\widetilde{\mathbf{u}},q_\Phi)_\Omega - (\nabla\cdot\mathbf{v}_\Phi,\widetilde{p})_\Omega \\ & +\frac{Pr}{\nu}(\mathcal{C}(\gamma)\widetilde{\mathbf{u}}\cdot\nabla T, S_\Phi)_\Omega \end{aligned}\right\} = 0, \quad \forall(\widetilde{\mathbf{u}},\widetilde{p}) \in (\mathcal{V}_0,\mathcal{P}). \tag{27}$$

and find $S_\Phi \in \mathcal{Q}_0$ such that

$$w^h\frac{1}{\Phi^h+\Delta^h}(1-\gamma,\widetilde{T})_\Omega + \left(K(\gamma)\nabla\widetilde{T},\nabla S_\Phi\right)_\Omega + \frac{Pr}{\nu}(\mathcal{C}(\gamma)\mathbf{u}\cdot\nabla\widetilde{T},S_\Phi)_\Omega = 0, \qquad \forall\widetilde{T}\in Q_0. \tag{28}$$

where $\mathbf{v}_\Phi, q_\Phi, S_\Phi$ are adjoint velocity, adjoint pressure, and adjoint temperature for the cost functional Φ.

For the integral form of TTG constraint(15), we have the following directional derivatives

$$\begin{aligned}
{\Psi^{I}}'_{\mathbf{u}}(\mathbf{u}, p, T, \gamma; \widetilde{\mathbf{u}}) =&0, && \text{(29a)}\\
{\Psi^{I}}'_{p}(\mathbf{u}, p, T, \gamma; \widetilde{p}) =&0, && \text{(29b)}\\
{\Psi^{I}}'_{T}(\mathbf{u}, p, T, \gamma; \widetilde{T}) =&2(\mathbf{t}\cdot\nabla T, \mathbf{t}\cdot\nabla\widetilde{T})_{\Gamma_{\mathrm{lc}}\cup\Gamma_{\mathrm{sc}}}. && \text{(29c)}
\end{aligned}$$

Plugging the above equations into (23) and (24), we have the following adjoint fluid equation and adjoint heat transfer equation for the TTG constraint Ψ^I: find $(\mathbf{v}_{\Psi^I}, q_{\Psi^I}) \in (\mathcal{V}_0, \mathcal{P})$ such that

$$\left.\begin{aligned}
&\mu(\nabla\widetilde{\mathbf{u}} + \nabla\widetilde{\mathbf{u}}^T, \nabla\mathbf{v}_{\Psi^I})_\Omega + \rho(\widetilde{\mathbf{u}}\cdot\nabla\mathbf{u} + \mathbf{u}\cdot\nabla\widetilde{\mathbf{u}}, \mathbf{v}_{\Psi^I})_\Omega\\
&\quad+(\alpha(\gamma)\widetilde{\mathbf{u}}, \mathbf{v}_{\Psi^I})_\Omega - (\nabla\cdot\widetilde{\mathbf{u}}, q_{\Psi^I})_\Omega - (\nabla\cdot\mathbf{v}_{\Psi^I}, \widetilde{p})_\Omega\\
&\quad+\frac{Pr}{\nu}(\mathcal{C}(\gamma)\widetilde{\mathbf{u}}\cdot\nabla T, S_{\Psi^I})_\Omega
\end{aligned}\right\} = 0, \quad \forall(\widetilde{\mathbf{u}}, \widetilde{p}) \in (\mathcal{V}_0, \mathcal{P}). \tag{30}$$

and find $S_{\Psi^I} \in \mathcal{Q}_0$ such that

$$2(\mathbf{t}\cdot\nabla T, \mathbf{t}\cdot\nabla\widetilde{T})_{\Gamma_{\mathrm{lc}}\cup\Gamma_{\mathrm{sc}}} + \Big(K(\gamma)\nabla\widetilde{T}, \nabla S_{\Psi^I}\Big)_\Omega + \frac{Pr}{\nu}\Big(\mathcal{C}(\gamma)\mathbf{u}\cdot\nabla\widetilde{T}, S_{\Psi^I}\Big)_\Omega = 0, \qquad \forall\widetilde{T}_0 \in Q. \tag{31}$$

where $\mathbf{v}_{\Psi^I}, q_{\Psi^I}, S_{\Psi^I}$ are adjoint velocity, adjoint pressure, and adjoint temperature for the integral TTG constraint Ψ^I.

In order to obtain the directional derivatives of the aggregated point-wise TTG constraint (18), we first obtain the directional derivative of its element constraint (17). Each constraint g_e consists of functions of some nodal temperature T_a^e and T_b^e (Fig. 2(b)). Its directional derivative with respect to T along $\widetilde{T}$ is a linear function of $\widetilde{T}$. That is

$${g_e}'_T(T; \widetilde{T}) = \frac{2(T_b^e - T_a^e)}{L_{ab}^2}\begin{bmatrix}-1 & 1\end{bmatrix}\begin{bmatrix}\widetilde{T}_a^e\\ \widetilde{T}_b^e\end{bmatrix}, \tag{32}$$

where e refers to e-th element's boundary, and $\widetilde{T}_a^e$ and $\widetilde{T}_b^e$ represent the test function for the adjoint system (or the variation of T) evaluated at node e_a and e_b, respectively. Thus g_e' corresponds to two point sources at nodes e_a and e_b. That is, we have point sources $2(T_b^e - T_a^e)/L_{ab}^2$ at node e_a and $-2(T_b^e - T_a^e)/L_{ab}^2$ at node e_b. This is equivalent to the source distribution, $2(T_b^e - T_a^e)/L_{ab}^2\delta(\mathbf{x} - \mathbf{v}_a^e)$, over the problem domain where $\delta(\mathbf{x})$ represents the Dirac delta function defined over the problem domain. Note the gradient is constant for all boundary points in each element edge due to the use of linear elements.

For aggregated point-wise TTG constraint (18), we thus have the following directional derivatives:

$${\Psi^{P}}'_{\mathbf{u}}(T; \widetilde{\mathbf{u}}) = 0, \tag{33}$$

$$\Psi^{P\prime}{}_p(T;\widetilde{p}) = 0, \tag{34}$$

$$\Psi^{P\prime}{}_T(T;\widetilde{T}) = \frac{1}{\sum_e \exp(pg_e)} \sum_e \exp(pg_e) g_e{}'_T(T;\widetilde{T}). \tag{35}$$

Plugging the above equations into (23) and (24), we have the following adjoint fluid equation and adjoint heat transfer equation for the TTG constraint Ψ^P (18): find $(\mathbf{v}_{\Psi^P}, q_{\Psi^P}) \in (\mathcal{V}_0, \mathcal{P})$ such that

$$\left.\begin{array}{l} \mu(\nabla\widetilde{\mathbf{u}} + \nabla\widetilde{\mathbf{u}}^T, \nabla\mathbf{v}_{\Psi^P})_\Omega + \rho(\widetilde{\mathbf{u}}\cdot\nabla\mathbf{u} + \mathbf{u}\cdot\nabla\widetilde{\mathbf{u}}, \mathbf{v}_{\Psi^P})_\Omega \\ \quad +(\alpha(\gamma)\widetilde{\mathbf{u}}, \mathbf{v}_{\Psi^P})_\Omega - (\nabla\cdot\widetilde{\mathbf{u}}, q_{\Psi^P})_\Omega - (\nabla\cdot\mathbf{v}_{\Psi^P}, \widetilde{p})_\Omega \\ \quad +\dfrac{Pr}{\nu}(\mathcal{C}(\gamma)\widetilde{\mathbf{u}}\cdot\nabla T, S_{\Psi^P})_\Omega \end{array}\right\} = 0, \quad \forall(\widetilde{\mathbf{u}}, \widetilde{p}) \in (\mathcal{V}_0, \mathcal{P}). \tag{36}$$

and find $S_{\Psi^P} \in \mathcal{Q}_0$ such that

$$\left.\begin{array}{l} \dfrac{1}{\sum_e \exp(pg_e)} \sum_e \exp(pg_e) g_e{}'_T(T;\widetilde{T}) \\ \quad + \Big(K(\gamma)\nabla\widetilde{T}, \nabla S_{\Psi^P}\Big)_\Omega + \dfrac{Pr}{\nu}(\mathcal{C}(\gamma)\mathbf{u}\cdot\nabla\widetilde{T}, S_{\Psi^P})_\Omega \end{array}\right\} = 0, \quad \forall\widetilde{T} \in \mathcal{Q}_0. \tag{37}$$

where $\mathbf{v}_{\Psi^P}$, q_{Ψ^P} and S_{Ψ^P} are adjoint velocity, adjoint pressure and adjoint temperature for the point-wise TTG constraint. The adjoint temperature S_{Ψ^P} also appears in the adjoint fluid equation. In (37), the constraint Ψ^P's derivative with regard to the temperature T would be used in the adjoint heat equation. This leads to point sources at nodes of boundary triangles containing each boundary facet.

4.4 Gradient representation

The directional derivative of the cost functional Φ with respect to design γ is

$$\Phi'_\gamma(\mathbf{u}, p, T; \widetilde{\gamma}) = w^f \frac{1}{\Phi^f + \Delta^f} \alpha'_\gamma(\gamma)(\mathbf{u}, \mathbf{u}\widetilde{\gamma})_\Omega - w^h \frac{1}{\Phi^h + \Delta^h}(T, \widetilde{\gamma})_\Omega.$$

Plugging this equation into (25), we have the total gradient as

$$\begin{aligned} \overline{\Phi}'_\gamma(\mathbf{u}, p, T, \gamma; \widetilde{\gamma}) = \quad & w^f \frac{1}{\Phi^f + \Delta^f} \alpha'_\gamma(\gamma)(\mathbf{u}, \mathbf{u}\widetilde{\gamma})_\Omega - w^h \frac{1}{\Phi^h + \Delta^h}(T, \widetilde{\gamma})_\Omega \\ & +(\alpha'_\gamma(\gamma)\mathbf{u}, \mathbf{v}_\Phi\widetilde{\gamma})_\Omega \\ & + \big(K'_\gamma(\gamma)\nabla T, \nabla S_\Phi\widetilde{\gamma}\big)_\Omega + \frac{Pr}{\nu}(\mathcal{C}'_\gamma(\gamma)\mathbf{u}\cdot\nabla T, S_\Phi\widetilde{\gamma})_\Omega + (K'_\gamma(\gamma)\bar{q}, S_\Phi\widetilde{\gamma})_{\Gamma_q}, \end{aligned} \tag{38}$$

where we have used the symbol $\overline{\Phi}'_\gamma(\mathbf{u}, p, T, \gamma; \widetilde{\gamma})$ to indicate the cost functional Φ's total gradient with respect to design γ.

The directional derivative of the integral form TTG Ψ^I (15) and point-wise TTG Ψ^P (18) with respect to design γ are

$$\Psi^{I\prime}_{\gamma}(\mathbf{u}, p, T; \widetilde{\gamma}) = 0,$$

and

$$\Psi^{P\prime}_{\gamma}(\mathbf{u}, p, T; \widetilde{\gamma}) = 0.$$

Thus, the total gradient of the integral form TTG with respect to design γ is

$$\begin{aligned}\overline{\Psi^I}'_\gamma(\mathbf{u}, p, T, \gamma; \widetilde{\gamma}) = \ & (\alpha'_\gamma(\gamma)\mathbf{u}, \mathbf{v}_{\Psi^I}\widetilde{\gamma})_\Omega \\ & + \left(K'_\gamma(\gamma)\nabla T, \nabla S_{\Psi^I}\widetilde{\gamma}\right)_\Omega + \frac{Pr}{\nu}(c'_\gamma(\gamma)\mathbf{u}\cdot\nabla T, S_{\Psi^I}\widetilde{\gamma})_\Omega + (K'_\gamma(\gamma)\bar{q}, S_{\Psi^I}\widetilde{\gamma})_{\Gamma_q}.\end{aligned} \tag{39}$$

Likewise, the total gradient of the point-wise TTG with respect to design γ is

$$\begin{aligned}\overline{\Psi^P}'_\gamma(\mathbf{u}, p, T, \gamma; \widetilde{\gamma}) = \ & (\alpha'_\gamma(\gamma)\mathbf{u}, \mathbf{v}_{\Psi^P}\widetilde{\gamma})_\Omega \\ & + \left(K'_\gamma(\gamma)\nabla T, \nabla S_{\Psi^P}\widetilde{\gamma}\right)_\Omega + \frac{Pr}{\nu}(\mathcal{C}'_\gamma(\gamma)\mathbf{u}\cdot\nabla T, S_{\Psi^P}\widetilde{\gamma})_\Omega + (K'_\gamma(\gamma)\bar{q}, S_{\Psi^P}\widetilde{\gamma})_{\Gamma_q}.\end{aligned} \tag{40}$$

5 Optimization algorithm

We use a gradient-based optimization algorithm to numerically seek an optimal design. During each iteration of the optimization process, the gradient of the cost function with respect to the design γ and the gradient of a TTG constraint with respect to the design are needed. Algorithm 1 illustrates the sequence for solving the primal PDEs, adjoint PDEs and the gradients during the optimization iteration. In each iteration, it needs to solve three sets of PDEs.

The first step in the algorithm is to solve the primal PDEs, including the fluid equation (5) to obtain $\mathbf{u}, p$, and the heat equation (11) to obtain T. The cost function (14) and a TTG constraint (15) or (18) can then be computed.

The next step is to then solve the adjoint PDEs for the cost function, including solving the adjoint heat problem (28) for S_Φ and the adjoint fluid problem (27) for $\mathbf{v}_\Phi, q_\Phi$. The cost function's gradient can be computed from (38) based on the computed S_Φ, $\mathbf{v}_\Phi$, and q_Φ.

The third set of PDEs are the adjoint PDEs for a TTG constraint, including the adjoint heat problem (31) for S_{Ψ^I} in the case of integral TTG (or (37) for S_{Ψ^P} in the case of point-wise TTG), and the adjoint fluid problem (30) for $\mathbf{v}_{\Psi^I}, q_{\Psi^I}$ (or (36) for $\mathbf{v}_{\Psi^P}, q_{\Psi^P}$). The TTG constraint's gradient (39) (or (40)) is then computed.

The two sets of adjoint PDEs, one for the cost function and the other for TTG constraint, can be solved in any order. Within each set of adjoint PDEs, the sequence for solving the adjoint heat problem and the adjoint fluid equation is reversed from that for solving the primal fluid equation and the primal heat equation. Among all the primal and adjoint equations, only the weak form of the primal Navier-Stokes equation (5) leads to non-linear equations of $\mathbf{u}$ and all other PDEs leads to linear equations.

Algorithm 1 Algorithm for solving the primal PDEs, adjoint PDEs and the gradients in optimization

for iter $\leq$ MaxIter & $|\Delta\boldsymbol{\gamma}|_\infty > 0.01$ **do**
    Solve the fluid problem (5) to obtain $\mathbf{u}, p$ ▷ Primal PDEs
    Solve the heat problem (11) to obtain T
    Compute cost function Φ from (14)
    Compute TTG Ψ^I from (15) or Ψ^P from (18)
    Solve the adjoint heat problem (28) for S_Φ ▷ Adjoint PDEs for Φ
    Solve the adjoint fluid problem (27) for $\mathbf{v}_\Phi, q_\Phi$
    Compute cost function's gradient (38)
    Solve the adjoint heat problem (31) for S_{Ψ^I} ▷ Adjoint PDEs for Ψ
        or (37) for S_{Ψ^P}
    Solve the adjoint fluid problem (30) for $\mathbf{v}_{\Psi^I}, q_{\Psi^I}$
        or (36) for $\mathbf{v}_{\Psi^P}, q_{\Psi^P}$
    Compute TTG constraint's gradient (39) or (40)
    Optimize to obtain updated design variables $\boldsymbol{\gamma}$
    Compute $\Delta\boldsymbol{\gamma}$
    iter +=1
end for

6 Numerical implementation and results

We present our numerical results based on optimized designs obtained under $Re = 50$ and $Re = 250$, i.e. laminar flow assumption. The domain is discretized with 10709 triangular elements, and the number of corner nodes are 5579, as shown in Fig. 3. For the Navier-Stokes equation and the two sets of adjoint fluid systems, Taylor-Hood elements are used. They are second order in velocity and first order in pressure. For temperature and density, linear elements are used. The solution of the PDEs is based on the open source finite element solver FEniCS [45]. The density is parameterized with 5579 nodal variables. The volume constraint is that the fluid should consume no more than 50% of the design domain. All the initial design variables are set to 0.5 so the initial volume constraint is active. The optimizer is the method of moving asymptotes [46]. In all examples below, the convergence criteria is the maximum change of nodal density γ should be smaller than 0.01 or the number of iterations reach 350. The ε in (18) starts with 1.2. It increases itself by 1.5 times after every 25 iterations until it reaches 10.

A Helmholtz partial differential equation based filtering is used. The Helmholtz filtering approach [31, 32] is a PDE-based realization of the common density filtering for ensuring

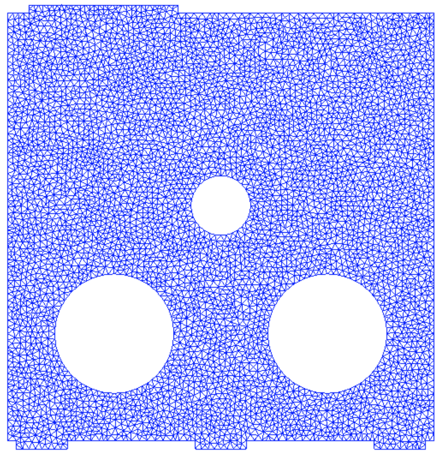

Figure 3: Total 10,709 triangular elements are used for the solution of PDEs.

length-scale control in topology optimization and it can be conveniently implemented [47] in generic finite element based software such as COMSOL and FEniCS. Isotropic Helmholtz PDE filtering can be described as

$$-r^2\nabla^2\overline{\gamma} + \overline{\gamma} = \gamma, \tag{41}$$

where r controls the size of the integral kernel and γ is the input design variable field and $\overline{\gamma}$ is the filtered density. In this paper, we have chosen $r = 0.1$. When the weight for the fluid objective is much larger than the weight for the heat, a stable optimized design can be obtained without extraneous filtering. This is consistent with the results from [33]. However, when the weight for the heat objective becomes dominant, filtering becomes necessary to avoid checkerboards. This is also consistent with [48].

In our implementation, the fluid is water with density $\rho = 998.21$ kg/m^3, viscosity $\mu = 1.002\text{e-}3$ kg/(m.s), thermal conductivity $k = 598.4 \times 10^{-3}$ W/(m.K), specific heat $c = 4.1818 \times 10^3$ J/(kg. K) and Prandtl number $Pr = 7.01$. The heat flux at the small tube is $\bar{q}_{\Gamma_{sc}} = 1000\ W/m$ and at the large tubes is $\bar{q}_{\Gamma_{sc}} = 10000\ W/m$. The solid is Aluminium with thermal conductivity $k = 205$ W/(m.K). The initial temperature is room temperature at $T_0 = 294.15K$.

6.1 Optimized designs at $Re = 50$

Figure 4 shows optimized designs and corresponding velocity and temperature distributions from different weights for fluid and heat objectives, under no TTG constraint and $Re = 50$. In the first row, the weights for the fluid and heat objectives are w^f=1e8 and w^h=1e-9, respectively. Due to the negligible weight for the heat objective, the combined optimization effectively reduces to the minimization of fluid power dissipation. Thus a very simple branching structure is obtained that consists of two “Y” structures to merge the flows from three inlets into one outlet. Due to the negligible weight for the heat objective, the resulting temperature is very high (up to 1.2e3). In the second row, the weights for the fluid and heat

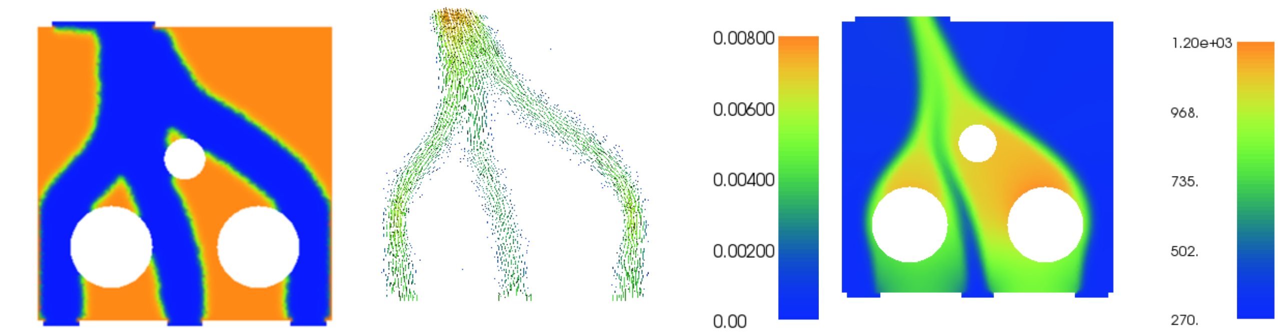

(a) Design, w^f=1e8, w^h=1e-9 (b) Velocity (c) Temperature

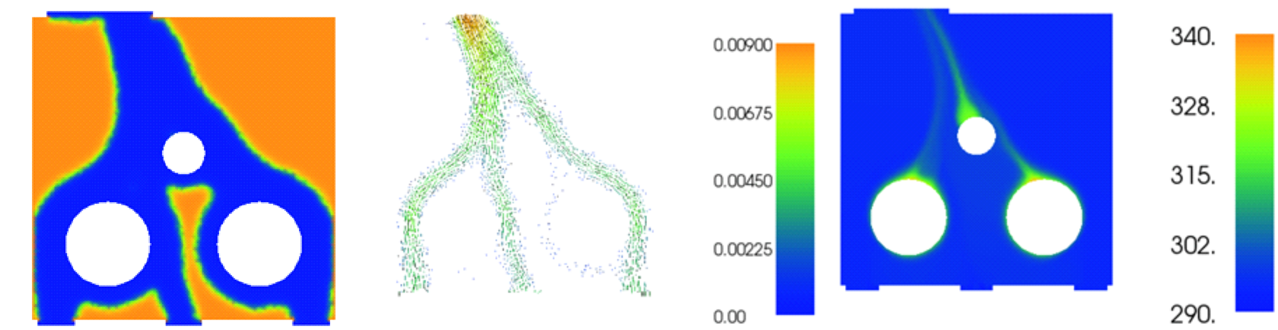

(d) Design, w^f=1e7, w^h=1e3 (e) Velocity (f) Temperature

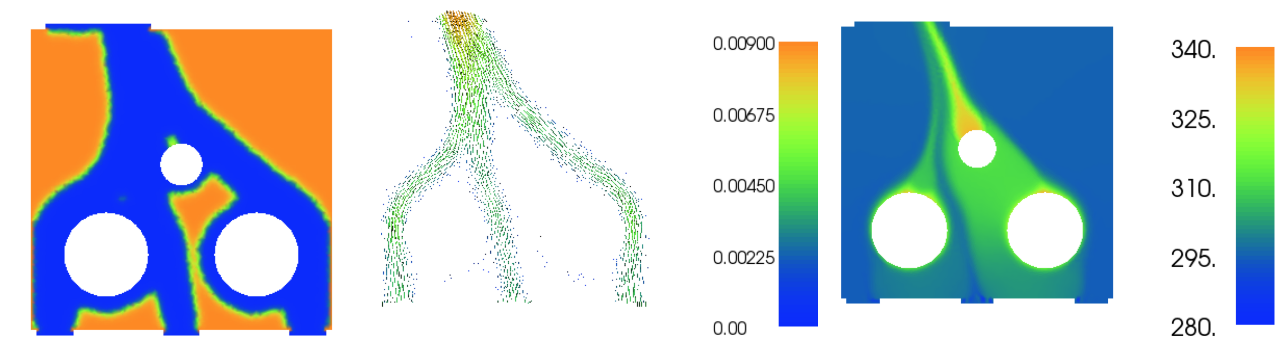

(g) Design, w^f=1e8, w^h=1e3 (h) Velocity (i) Temperature

Figure 4: Optimized designs and corresponding velocity and temperature distributions from different weights for fluid and heat objectives, under no TTG constraint and $Re = 50$.

objectives are w^f=1e7, w^h=1e3. Due to the relatively high weight for the heat objective, large circular fluid paths are obtained around the full circumference of each heat-generating tube. In the third row, the weights for the fluid and heat objectives are w^f=1e8, w^h=1e3. This leads to improved heat transfer and reduced fluid power dissipation in the optimized designs. However, in all three designs, due to the lack of TTG constraints, there is substantial TTG that are visible along the tube boundary. For example, in the left tube in Fig. 4(f), there is sharp transition between high temperature and lower temperature along the boundary of the left tube.

In order to overcome high TTG along the tube boundary, TTG constraints, either the integral form or the point-wise form, have been imposed. Figure 5 compares the design in Fig. 4(g) without TTG constraints with the designs with TTG constraints, and displays the corresponding detailed TTG profiles along the three tubes in each design. In the TTG profiles (right column) in Fig. 5, the x-axes represents the degree counter-clock-wise along each tube, starting from right most point in each tube. Each point in the profile represents the TTG of one element. Comparing subfigures in the second column and the third column, the temperature in the first row (w/o TTG constraint) has high TTG around the small tube and two large tubes. With the TTG constraints, high TTGs have been suppressed. Figure 5(c) shows the highest pointwise TTG (-7235) at 151° of the small tube. By invoking the integral TTG constraint (2nd row) of $\theta^I = 0.0043$, the TTGs of all three tubes have been reduced, with maximum TTG (2987) at the 137° of the right large tube. By invoking the pointwise TTG constraint (3rd row) of $\theta^P = 0.65$, the pointwise TTG has been reduced to about one fourth of that in Fig. 5(c), with the largest pointwise TTG (1856) occurring at elements of both left and right large tubes. Comparing Fig. 5(f) and (i), although the integrals of squared TTG along the boundaries are the same, the pointwise TTG constraint avoids local spike in TTG.

Table 1: Fluid and thermal performances for various optimized designs with $Re = 50$

	Fluid power dissipation Φ^f	Temperature Φ^h	TTG Ψ^I	$\mathbf{t} \cdot \nabla T$ (max)
$w^f = 1e8, w^h = 1e\text{-}9$	0.237	0.4764	3.2634	4.855
$w^f = 1e7, w^h = 1e3$	0.308	0.2293	0.0131	0.766
$w^f = 1e8, w^h = 1e3$	0.280	0.2308	0.0133	0.260
$w^f = 1e8, w^h = 1e3$ θ^I =0.0043	0.252	0.2327	0.0043	0.107
$w^f = 1e8, w^h = 1e3$, $\theta^P = 0.65$	0.299	0.2308	0.0043	0.066

Table 1 quantitatively compares the fluid and thermal objectives in the above optimized designs as well as the corresponding integral TTG quantity and pointwise the maximum TTG quantity along the boundary. All numerical values in the table are relative to the initial design. At the initial design where $\gamma = 0.5$ throughout the design domain, the fluid power dissipation is $\Phi_0^f = 1.061e - 5$, the overall temperature is $\Phi_0^h = 5.5105$, the integral form of TTG is $\Psi_0^I = 3.90e7$, and point-wise maximum TTG is $\Psi_0^P = 2.78e4$. With the large weight for the fluid objective (1st row), the fluid objective is small (only 23.7% of initial design). However the overall temperature is 47.64% of the initial design. More importantly, the TTG is several ($3 \sim 4$) times larger than the initial design. This is because the flow path does not circle around the heating tubes, as shown in Fig. 4(a). With the large weight for the heat objective (2nd row), the temperature is only 22.93% of the initial design with much smaller TTG than the design in the 1st row. However, the fluid power dissipation becomes 30.8% of the initial design. A compromise is made when the weights are $w^f = 1e8, w^h = 1e3$. In this case, the fluid power dissipation is 28.0% of the initial design and the temperature is 23.08%. The TTG is also smaller. In order to further control the TTG, both forms of TTG constraints can be imposed. In order to compare the effects of the two forms of TTG constraints, we have chosen θ^P and θ^I so that the integrals of squared TTGs are the same in both cases. The integral constraint $\theta^I = 0.0043$ leads to the optimized design with maximum pointwise TTG 10.7% of the initial design. The pointwise constraint $\theta^P = 0.65$ leads to the optimized design with 6.6% TTG of the initial design. Thus, the two ways of constraining TTG are both effective and they make the integral TTG to be 0.43% of the initial design and pointwise TTG to be below 11%. This can also be seen from Fig. 5(e) and (h), the temperature along the tube boundaries transition smoothly. In addition, the pointwise TTG constraint leads to smaller maximum pointwise TTG than the integral TTG constraint.

Figure 6 also shows the convergence history of the optimized design in Fig. 5(g). It takes 202 iterations for this particular design. The fluid power dissipation, the temperature over the design domain and the TTG (pointwise) and the volume of the fluid are plotted with respect to the iteration.

6.2 Optimized designs at $Re = 250$

Figure 7 shows a set of optimized designs at $Re = 250$ without any TTG constraint with varying weights for the fluid objective and the same weight for the heat objective ($w^h = 1e3$). The second and third row in Fig. 7 display the corresponding velocity and temperature distribution. It is clear that with the decrease of weight for fluid objectives, the optimized designs become more complex and larger circular flow paths along the tubes appear. When $w^f = 1e8$, an optimized design that connects the inlets directly with the outlet, without circling around the tubes, appears. Comparing this design with a similar design in Fig. 4(a) where $Re = 50$, it can be seen that flow paths from different inlets merge further away from the tubes at Re=250. This is due to the increase of the flow speed and fluid momentum. A more quantitative analysis of the fluid and heat objectives, along with the integral and pointwise TTG is detailed in Table 2. It can be seen from this table that, with the decrease of w^f, the rate of fluid power dissipation with respect to the initial design increases and the overall temperature decreases along with the TTG about the tubes.

For the design in Fig. 7(g), we plot the temperature distribution and its TTG along the tubes in the 1st row of Fig. 8. The next two rows of Fig. 8 display the optimized designs under TTG constraints. The 2nd row shows the design under integral TTG constraint $\theta^I = 0.0086$ and the 3rd row under pointwise TTG constraint $\theta^P = 0.65$. Without TTG

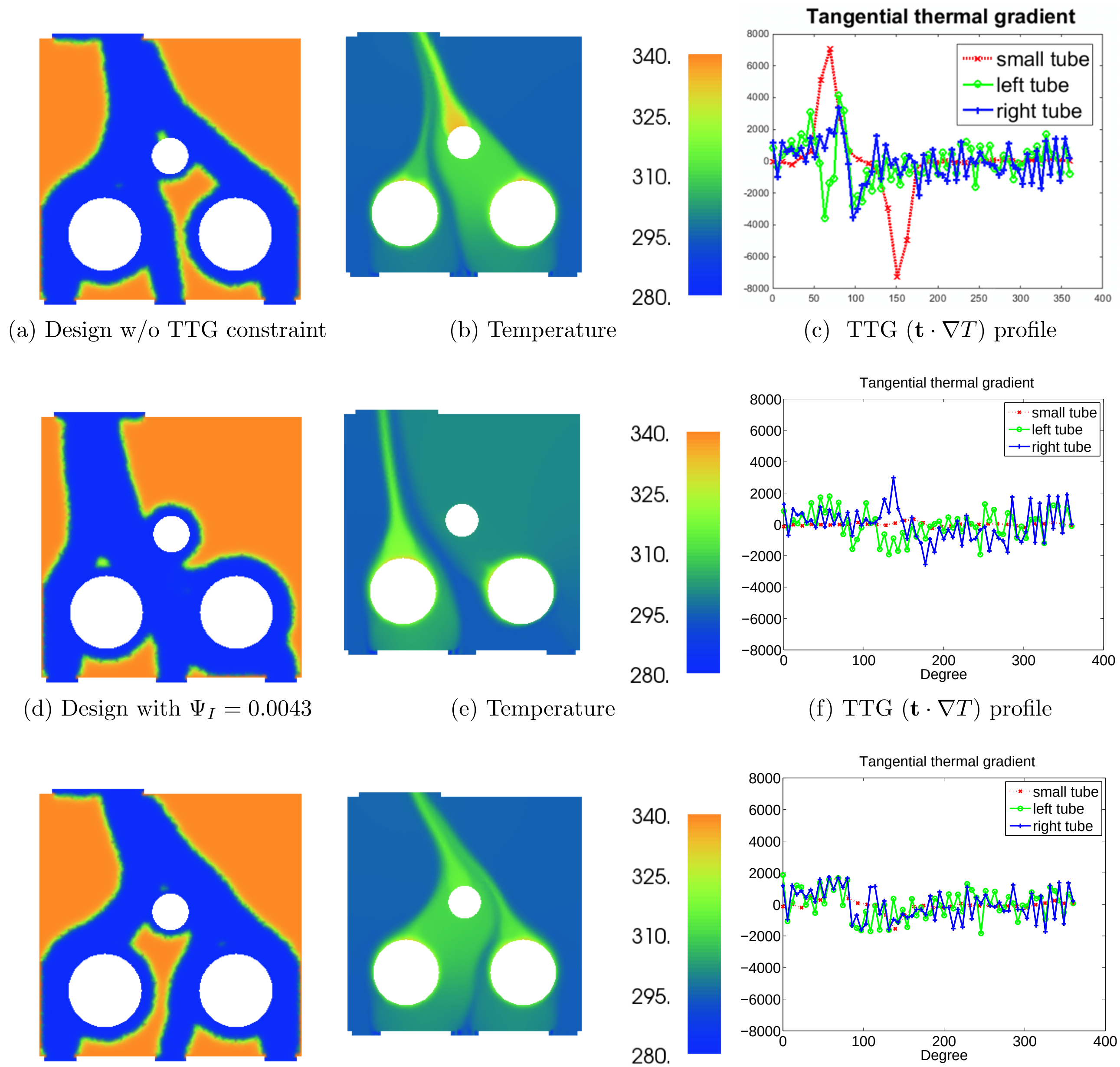

(a) Design w/o TTG constraint (b) Temperature (c) TTG ($\mathbf{t} \cdot \nabla T$) profile

(d) Design with $\Psi_I = 0.0043$ (e) Temperature (f) TTG ($\mathbf{t} \cdot \nabla T$) profile

(g) Design with $\Psi_p = 0.65$ (h) Temperature (i) TTG ($\mathbf{t} \cdot \nabla T$) profile

Figure 5: Optimized designs and temperature distributions at $Re = 50$ and $w^f = 1e8, w^h = 1e3$, without TTG constraint (1st row), with integral TTG constraint $\theta^I = 0.0043$ (2nd row) and with pointwise TTG constraint $\theta^P = 0.65$ (3rd row).

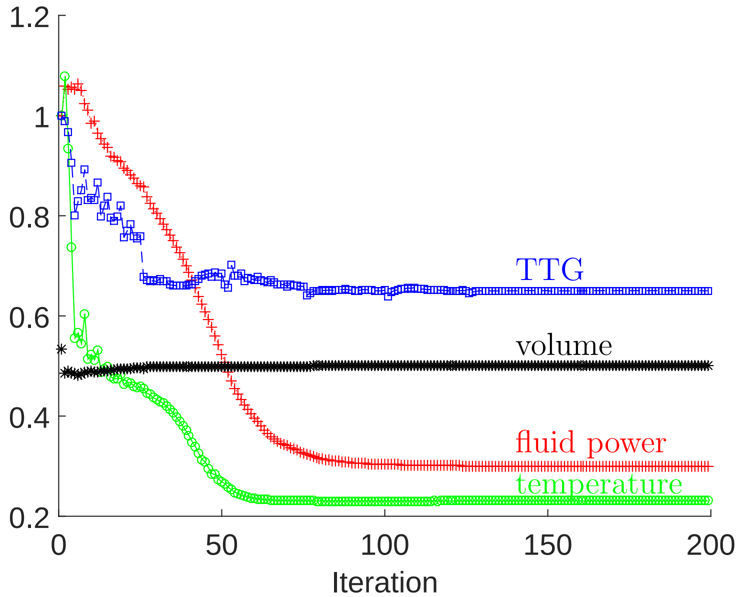

Figure 6: Convergence history for the optimization in Fig. 5(g)

constraint, the maximum TTG (6735) occurs at 51° of the right tube in Fig. 8(c). With integral TTG constraint $\theta^I = 0.0086$, the maximum TTG (-2862) occurs at 325° of the right tube. With pointwise TTG constraint $\theta^P = 0.65$, the maximum TTG (1291) occurs along many elements of the right and left tubes. Comparing Fig. 8(f) and (i), although the integrals of the squared TTG along the boundaries are the same, the pointwise TTG constraint avoids local spike in TTG and produces near uniform pointwise TTG.

The performances in fluid and heat objectives as well as TTGs in four designs without TTG constraints and the two designs with TTG constraints are summarized in Table 2. All numerical values in the table are relative to the initial design. At the initial design where $\gamma = 0.5$ throughout the design domain, the fluid power dissipation is $\Phi_0^f = 4.61e-4$, the overall temperature is $\Phi_0^h = 2.95$, the integral form of TTG is $\Psi_0^I = 1.64e7$, and point-wise maximum TTG along the tube boundaries is $\Psi_0^P = 1.65e4$. Again, it is clear that lower weights for the fluid objective lead to higher percentage of fluid power dissipation and lower temperature in the design domain. The TTG constraints are effective in controlling the TTG along the tubes.

6.3 Geometric effects of the TTG constraint

The previous examples at Re=50 and Re=250 demonstrate that, with and without TTG constraints, optimized designs have very different shapes and topologies when initial designs are represented with uniform density $\gamma = 0.5$. This is due to the existence of multiple local minimums for the optimization problem. During the first few iterations, the designs usually do not satisfy the TTG constraints. Thus, optimization, with and without TTG constraints, leads to different evolution of density distributions during the optimization process, thus

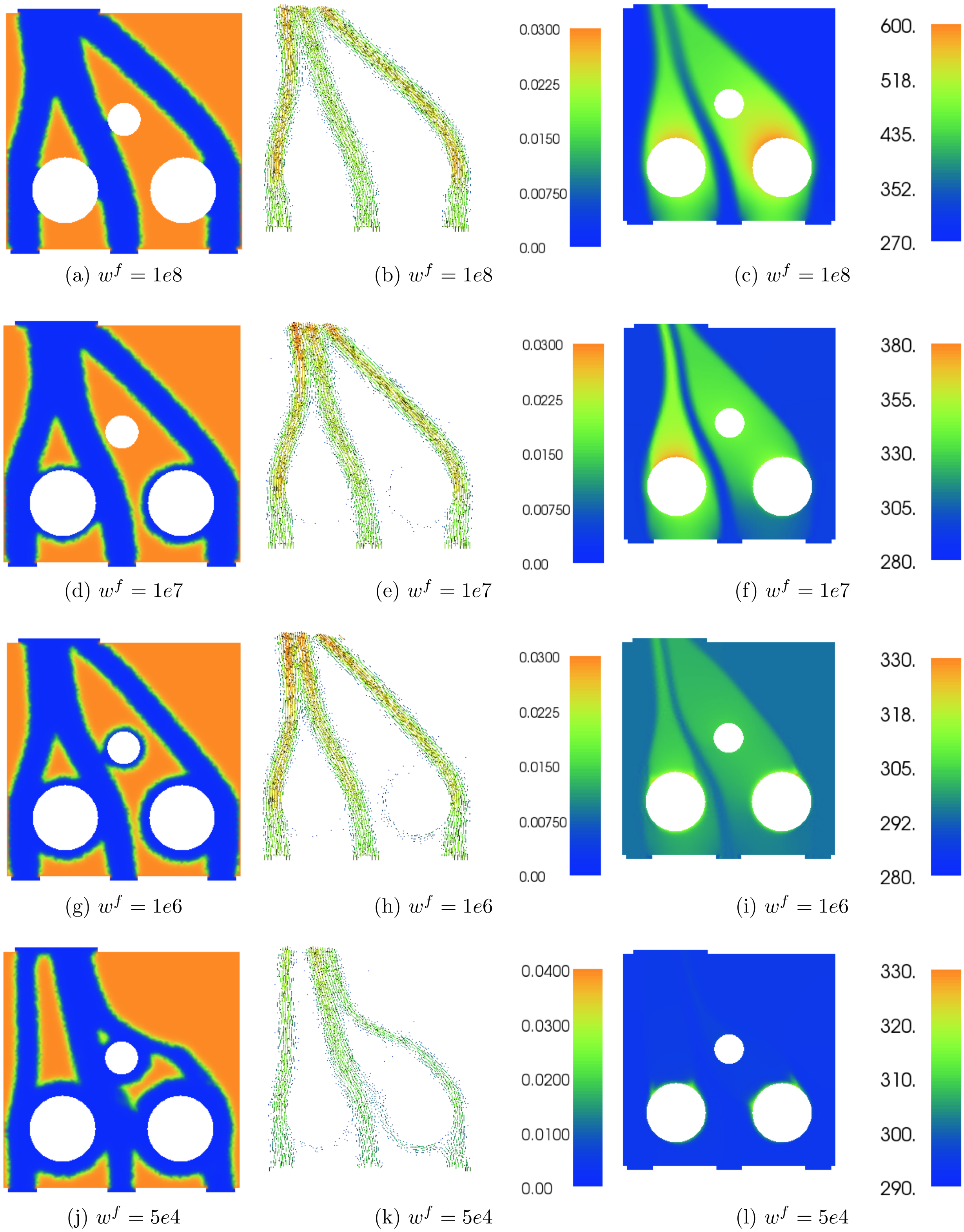

Figure 7: Optimized designs from different weight for fluid w^f and same weight for heat $w^h = 1e3$ under no TTG constraint and $Re = 250$.

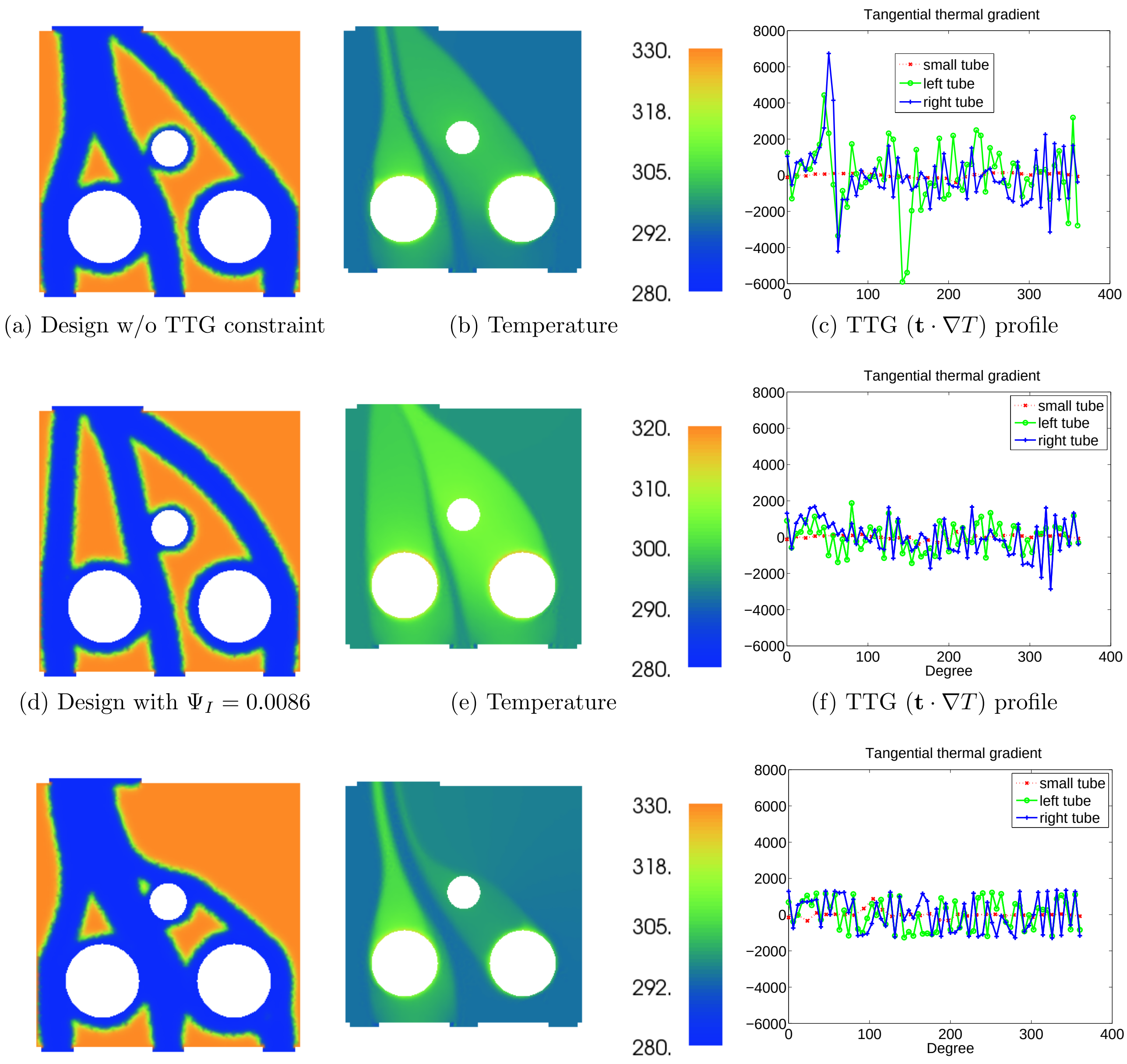

(a) Design w/o TTG constraint (b) Temperature (c) TTG ($\mathbf{t} \cdot \nabla T$) profile

(d) Design with $\Psi_I = 0.0086$ (e) Temperature (f) TTG ($\mathbf{t} \cdot \nabla T$) profile

(g) Design with $\Psi_p = 0.65$ (h) Temperature (i) TTG ($\mathbf{t} \cdot \nabla T$) profile

Figure 8: Optimized designs and temperature distributions at $Re = 250, w^f = 1e6, w^h = 1e3$ without TTG constraint, with integral TTG constraint $\theta^I = 0.0086$ (2nd row) and pointwise TTG constraint $\theta^P = 0.65$ (3rd row).

Table 2: Fluid and thermal performances for various optimized designs with $Re = 250$, $w^h = 1e3$

	Fluid power dissipation Φ^f	Temperature Φ^h	TTG Ψ^I	$\mathbf{t} \cdot \nabla T$ (max)
$w^f = 1e8$	0.208	0.6255	1.4885	2.534
$w^f = 1e7$	0.234	0.4506	0.0678	0.781
$w^f = 1e6$	0.278	0.4320	0.0303	0.408
$w^f = 5e4$	0.380	0.4286	0.0281	0.356
$w^f = 1e6, \theta^I = 0.0086$	0.299	0.4336	0.0086	0.173
$w^f = 1e6, \theta^P = 0.65$	0.275	0.4309	0.0086	0.078

different optimized designs after convergence. In order to further understand the geometric effects of TTG constraints on the designs, we choose the optimized designs obtained without TTG constraints as initial designs for optimization with TTG constraints. The results are shown in Fig. 9 and Fig. 10, respectively, for $Re = 50$ and $Re = 250$.

Figure 9 shows three sets of designs obtained with Re=50, $w^f = 1e8$ and $w^h = 1e$-9, $5e1$ and $1e3$, respectively. These three sets of designs are shown in three rows, respectively. In the first column are the initial designs obtained from optimization without TTG constraints. They are then optimized under integral form TTG constraint (0.2%) and the optimized designs are shown in the 2nd column. The density differences between the optimized designs (2nd column) and the initial designs (1st column) are shown in the 3rd column. Figure 9(a) shows an initial design obtained with extremely small weight for the heat objective, thus leading to no flow at the back of large tubes. After optimization with TTG constraint, flows appear at the back of the large tubes shown in Fig. 9(b). As we increase the heat weight for the initial design shown in Fig. 9(d), more flow appears around the large tubes. However, there is still solid near the back of the large right tube, leading to large TTG at the back of the large right tube. With the TTG constraint, a closed flow path around the right tube is formed. With the further increase of the heat objective for the initial design (Fig. 9(g)), full circular flows occur for two large tubes and a small solid spot occurs at the back of the small tube. Optimization with the TTG constraint leads to more fluid added at the original solid spot and forms full flow path around the small tube. On the other hand, for the large tubes, very little change occurs in the flow path shape. This is because, with the high heat weight and the resulting full flow path, the TTG is already relatively small around the large tubes.

Figure 10 shows three sets of designs obtained with Re=250, $w^h = 1e3$ and $w^f = 1e8, 1.8e7$ and $1e6$, respectively. These three sets of designs are shown in three rows, respectively. The initial designs (1st column) obtained without TTG constraints are optimized under integral form of TTG constraints (0.3%). The results are shown in the 2nd column and the density differences in the 3rd column. When the initial design is obtained with high weight for the fluid objective, Fig. 10(a), there is no flow circling around the tubes and high

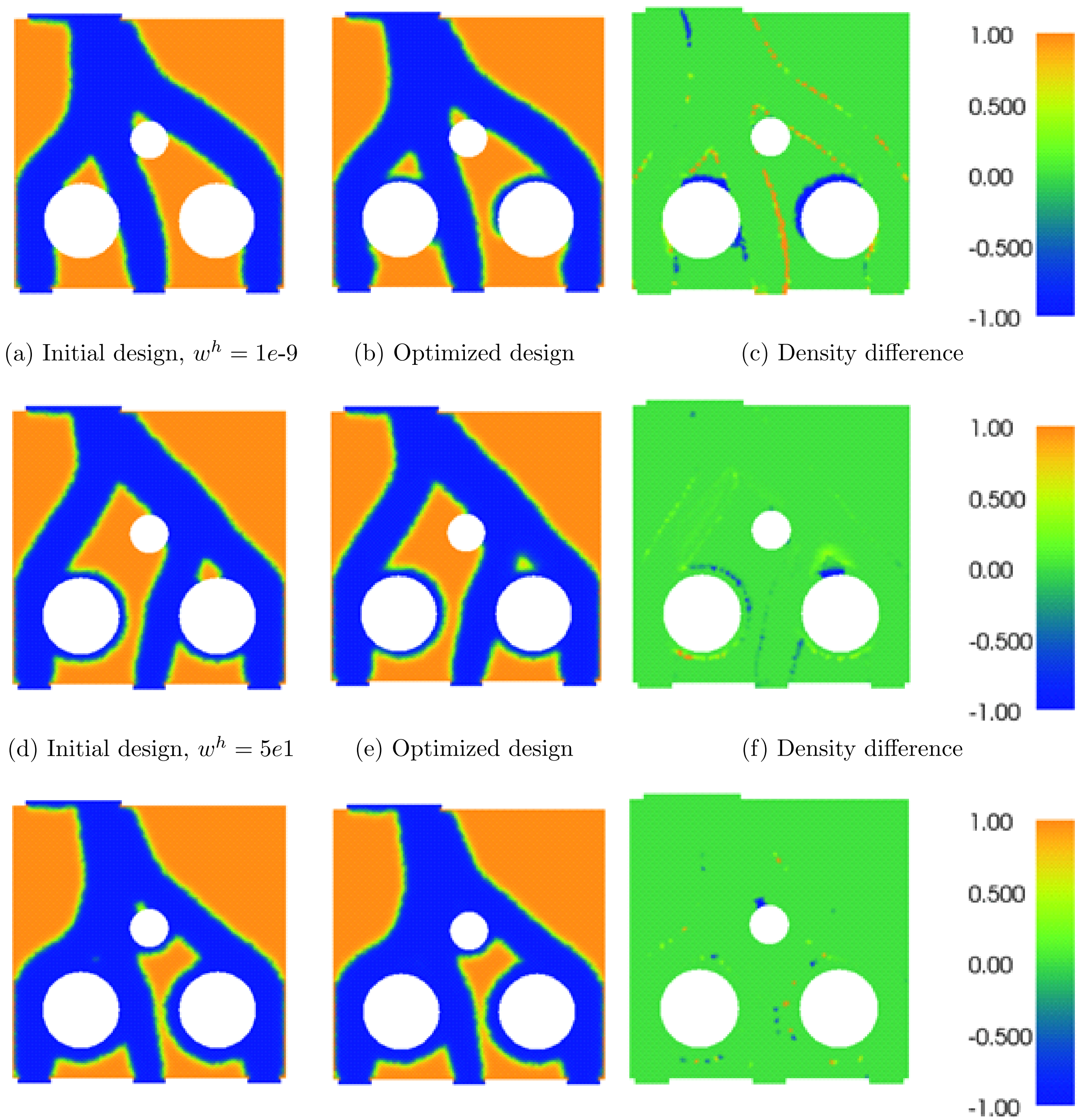

(a) Initial design, $w^h = 1e\text{-}9$ (b) Optimized design (c) Density difference

(d) Initial design, $w^h = 5e1$ (e) Optimized design (f) Density difference

(g) Initial design, $w^h = 1e3$ (h) Optimized design (i) Density difference

Figure 9: Optimized designs without any TTG constraint (1st column) are used as initial designs for optimization under integral TTG constraint. The results are shown in the 2nd column and the density difference between the designs are shown in the 3rd column, respectively, $w^f = 1e8$ and Re=50 in all cases.

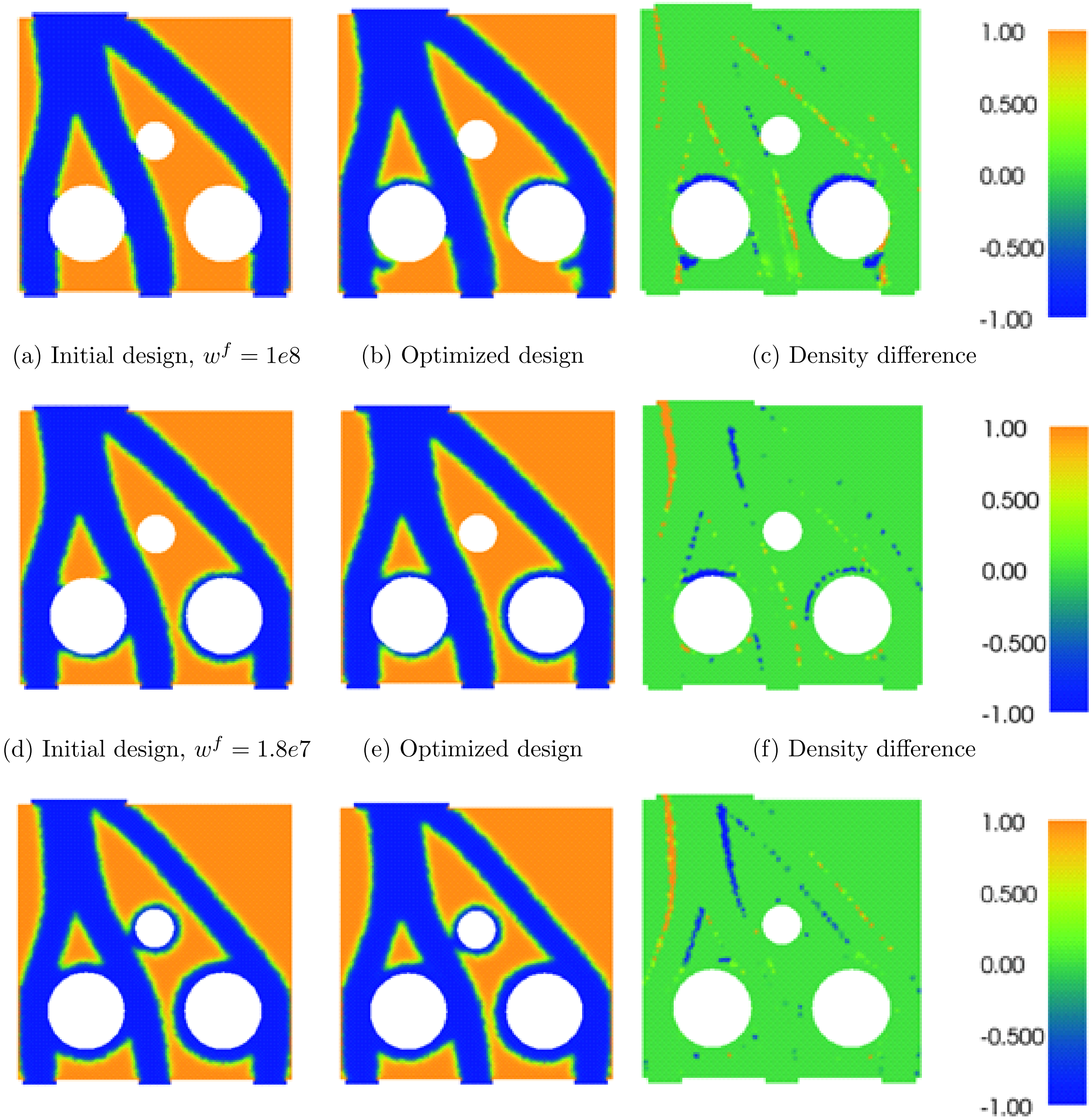

(a) Initial design, $w^f = 1e8$ (b) Optimized design (c) Density difference

(d) Initial design, $w^f = 1.8e7$ (e) Optimized design (f) Density difference

(g) Initial design, $w^f = 1e6$ (h) Optimized design (i) Density difference

Figure 10: Optimized designs without any TTG constraint (1st column) are used as initial designs for optimization under integral TTG constraint. The results are shown in the 2nd column and the density difference between the designs are shown in the 3rd column, respectively. $w^h = 1e3$ and Re=250 in all cases.

TTG occurs at the back of the large tubes. After the TTG constraint is imposed, circular flow paths at the back of the large tubes appear. In Fig. 10(d), high TTG exists at the back of the left, large tube. The TTG constraint leads to full flow around the left, large tube, shown in Fig. 10(e). In Fig. 10(g), the initial design is obtained with relatively small fluid weight, full flow paths exist in all three tubes. As a result, the TTG is relatively small. With the TTG constraint, there is very little change in flows near the tubes.

Therefore, the above two examples at Re=50 and Re=250 demonstrate that the geometric effect of the TTG constraint is most obvious when there is initially incomplete flow path around the tubes. The lack of flow at the back of the tubes leads to high TTG and optimization with the TTG constraint then adds fluid at the back of the tubes. When there is initially large wide circular flow around the tubes, the TTG is already relatively low around the tubes. Therefore the geometric change around the tubes due to the TTG constraints is small perturbation of wall boundary. This can be seen from sporadic dots around the tubes shown in Fig. 9(i) and Fig. 10(i).

7 Discussions

7.1 Oscillation and mesh refinement

Since the optimization in this paper concerns TTG constraints in a thermofluid system, it is important to ensure the temperature and TTG are properly modelled. Some of analysis results presented so far exhibit oscillation in both temperature and in gradient. For example, the TTG profile in Fig. 5(a) exhibits oscillation. Such oscillation can be resolved through finer boundary layer mesh or through stabilization techniques. Figure 11 shows the design in Fig. 5(a) is reanalyzed with a denser mesh. It consists of 21736 triangular elements, adaptively distributed with finer elements around the tubes. The resulting TTG profiles are shown in Fig. 11(b). Comparing Fig. 5(c) and Fig. 11(b), it can be seen that the oscillation in TTG has been removed due to the use of dense boundary layer elements around the tubes. However, the solution from the original mesh did capture overall trend of the TTG profiles around the tubes. If the mesh is too coarse and there is too much oscillation in TTG profiles, the optimization may not lead to useful designs.

Figure 12 shows a set of optimized designs obtained from two meshes: mesh 1 has 10709 elements as shown in Fig. 3 and mesh 2 has 21736 adaptive elements as shown in Fig. 11. The weights are $w^f = 1e8$ and $w^h = 5e1$ for all designs. Fig. 12(a) and (b) correspond to designs in Fig. 9(d) and (e), obtained with mesh 1. If we use the design in Fig. 9(d) as initial design for optimization with mesh 2 under the integral form of TTG constraint (0.2%), the resulting design is shown in Fig. 12(c). Comparing Fig. 12(b) from mesh 1 and Fig. 12(c) from mesh 2, the designs are nearly identical, except finer wall boundary near the tubes due to the use of more elements. Figure 12(d) shows the optimized design with mesh 2, without TTG constraints. The design is then used as initial design for optimization with TTG constraint and the result is shown in Fig. 12(e). The density difference between the two designs is shown in Fig. 12(f). Again, the TTG constraints add fluid path around the

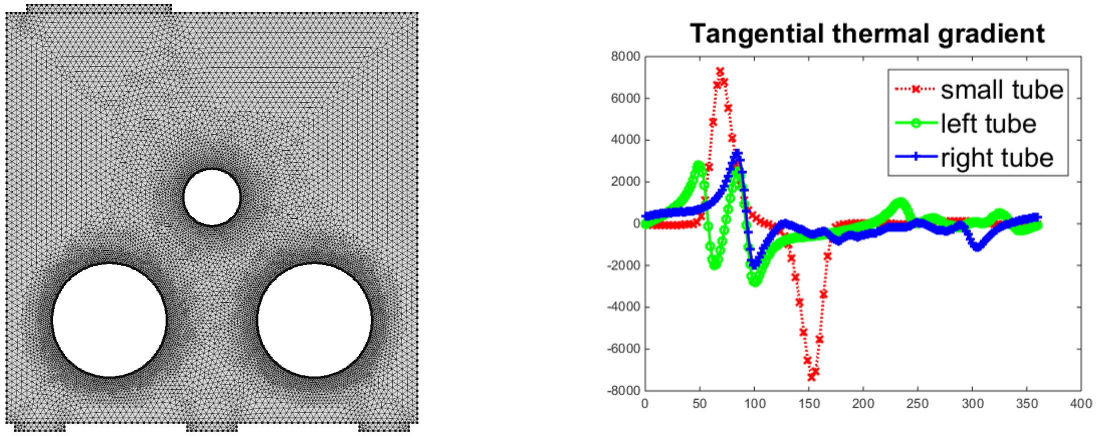

(a) 21736 adaptive elements

(b) TTG from design in Fig. 5(a)

Figure 11: A new mesh consisting of 21736 adaptive elements is used to reanalyze the design in Fig. 5(a). The resulting TTG around the tubes are shown in figure (b).

(a) Initial design from mesh 1

(b) Optimized design from mesh 1

(c) Optimized design from Mesh 2

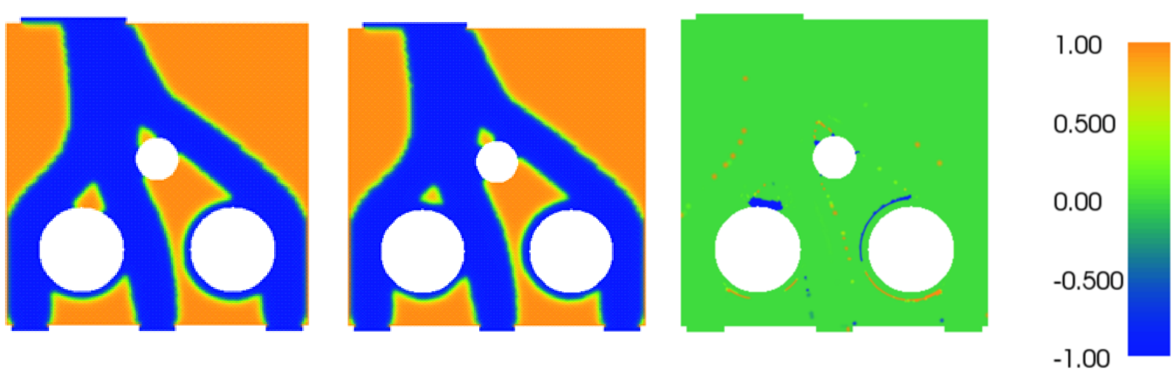

(d) Initial design from mesh 2

(e) Optimized design from mesh 2

(f) Density difference

Figure 12: Optimized designs from mesh 1 and 2.

left tube in Fig. 12(d) to reduce TTG. The difference between Fig. 12(c) and Fig. 12(e) are likely due to the existence of multiple local minimum. This example suggests that the optimized designs from mesh 1 are similar to designs obtained with finer mesh. This can be ascribed to the fact that mesh 1 is dense enough to capture the overall trend of temperature and TTG distributions.

7.2 Material interpolation

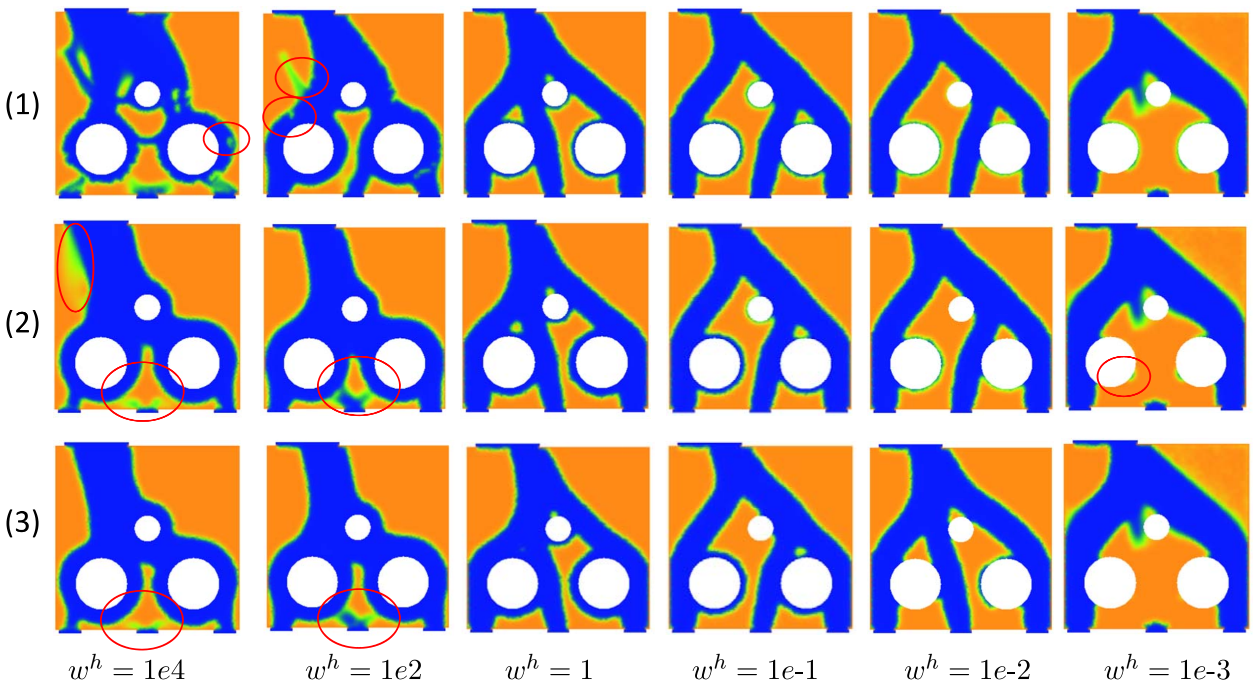

Figure 13: Optimized designs with different material interpolations for thermal conductivity.

In all designs presented so far, clear fluid/solid contrast has been obtained. We discuss below when the contrast may fade and the effect of different forms of material interpolation for thermal conductivity.

The material interpolation for thermal conductivity is based on (7), where $p_k = 3$ for all examples so far. This interpolation equation leads to higher than linearly interpolated thermal conductivity for intermediate density, when $p_K > 1$. Our choice of such a particular form of material interpolation is based on analysis of our numerical results. Here we present a set of numerical results based on different forms of interpolation. The first interpolation is

$$K(\gamma) = 1 + (1-\gamma)^{p_k}(K_0 - 1), \tag{42}$$

where $p_k = 3$. This interpolation follows the usual SIMP procedure where thermal conductivity is *penalized* for intermediate density. The second form of interpolation is just linear interpolation and has $p_k = 1$. In this case, (7) and (42) are equivalent. The third form is the one presented earlier, based on (7), with $p_k = 3$. Optimized designs under these three forms of material interpolation functions for thermal conductivity are compared in Fig. 13 for flow at Re=50. The designs in the first row are based on (42) with $p_{\mathcal{C}} = p_k = 3$. The designs in the second row have $p_{\mathcal{C}} = p_k = 1$. The designs in the third row are based on (7) with $p_{\mathcal{C}} = p_k = 3$. In all examples, the material interpolation for Darcy friction coefficient $\alpha(\gamma)$ still follows (4) with the same penalization parameter $q = 0.1$. In all designs, the weight for the fluid objective is $w^f = 1e5$. From the left to the right of this figure, the weight for the heat objective decreases from $1e4$ to $1e$-3. This numerical experiment suggests the following:

1. When the weights are appropriate, e.g. for $w^h = 1$ or $1e$-1, good designs with clear solid/fluid contrast are obtained for all three forms of thermal conductivity interpolation. However, the thermal conductivity interpolation (42) (penalizing the intermediate density) leads to smaller fluid flow paths around the tubes than the linear interpolation does, and even smaller paths than the interpolation based on (7) does. It also appears that the interpolation based on (7) has the effect of suppressing tiny flow paths around the tubes. For example, in the 1st row and 2nd row, for $w^h = 1e$-1, there are small flow paths around the small tubes. However, the small flow path does not appear in the 3rd row.

2. With the heat weight is low, at $w^h = 1e$-3, linear interpolation (2nd row) leads to an isolated fluid.

3. With the increase of the weight for heat objective, $w^h = 1e2$, the clear fluid/solid contrast begins to fade for all three forms of interpolation. A small fluid branch appears for the first form of interpolation based on (42).

4. When the weight for the heat objective becomes even larger, i.e. $w^h = 1e4$, all three forms of interpolation leads to broken flow paths that fail to completely connect with the middle inlet. The interpolation based on (42) shown in the first row leads to unclear flow paths around the tubes. The linear interpolation of thermal conductivity also leads to intermediate density around the outlet, as highlighted in the 2nd row. With the interpolation of thermal conductivity based on (7), further increase of heat weight beyond 1e4 does not change the topology.

Overall, thermal conductivity interpolation based on (7) leads to more stable designs. We have also experimented with the penalty coefficient $p_{\mathcal{C}}$ and find it has no strong effect on the optimized designs when $p_{\mathcal{C}}$ is between 1 and 3.

8 Conclusions

This paper presents a continuous adjoint approach to topology optimization of a coupled thermal-fluid system under tangential thermal gradient constraints. We have derived three sets of adjoint equations, adjoining a weighted sum of thermal objective (minimal temperature) and fluid objective (minimal fluid power dissipation) and two TTG constraints with the governing Navier-Stokes equations and heat transfer equations. It leads to three sets of adjoint PDEs and gradient expressions. Our derivation of adjoint systems and gradient expressions is general in the sense that it is applicable to any functionals of domain integral, boundary integral or pointwise quantities under thermal-fluid governing equations.

Numerical examples demonstrate that the continuous adjoint approach leads to successful topological optimization of a constrained thermal-fluid system. The use of TTG constraint is effective in lowering the TTG along the heat source boundaries. The resulting designs exhibit clear black/white contrast. The proposed optimization formulation may be useful in practical design of shell and tube heat exchangers or water jacket design for precise temperature control.

Our continuous adjoint approach to handling the sensitivity of the cost function and two forms of TTG constraints can be extended to transient problems in a way that is similar to how continuous adjoint is used in optimizing unsteady Navier-Stokes flow [25, 26].

Acknowledgement

The first author wants to acknowledge the support from the National Science Foundation grant #1435072. The authors are thankful for reviewers' thorough and constructive feedback.

References

[1] M.P. Bendsoe and N. Kikuchi. Generating optimal topologies in structural design using a homogenization method. *Computer Methods in Applied Mechanics and Engineering*, 71(2):197–224, 1988.

[2] M.P. Bendsøe and O. Sigmund. *Topology Optimization: Theory, Methods, and Applications*. Springer Verlag, 2003.

[3] Joshua D Deaton and Ramana V Grandhi. A survey of structural and multidisciplinary continuum topology optimization: post 2000. *Structural and Multidisciplinary Optimization*, 49(1):1–38, 2014.

[4] Martin P Bendsøe. Optimal shape design as a material distribution problem. *Structural optimization*, 1(4):193–202, 1989.

[5] M Zhou and GIN Rozvany. The coc algorithm, part ii: topological, geometrical and generalized shape optimization. *Computer Methods in Applied Mechanics and Engineering*, 89(1):309–336, 1991.

[6] HP Mlejnek. Some aspects of the genesis of structures. *Structural Optimization*, 5(1-2):64–69, 1992.

[7] Grégoire Allaire, François Jouve, and Anca-Maria Toader. Structural optimization using sensitivity analysis and a level-set method. *Journal of computational physics*, 194(1):363–393, 2004.

[8] Michael Yu Wang, Xiaoming Wang, and Dongming Guo. A level set method for structural topology optimization. *Computer methods in applied mechanics and engineering*, 192(1):227–246, 2003.

[9] J Sokolowski and A Zochowski. On the topological derivative in shape optimization. *SIAM Journal on Control and Optimization*, 37(4):1251–1272, 1999.

[10] Krishnan Suresh. Efficient generation of large-scale pareto-optimal topologies. *Structural and Multidisciplinary Optimization*, 47(1):49–61, 2013.

[11] Blaise Bourdin and Antonin Chambolle. Design-dependent loads in topology optimization. *ESAIM: Control, Optimisation and Calculus of Variations*, 9:19–48, 2003.

[12] YM Xie and Grant P Steven. A simple evolutionary procedure for structural optimization. *Computers & structures*, 49(5):885–896, 1993.

[13] Ercan M Dede. Multiphysics topology optimization of heat transfer and fluid flow systems. In *proceedings of the COMSOL Users Conference*, 2009.

[14] Ercan M Dede. Multiphysics optimization, synthesis, and application of jet impingement target surfaces. In *Thermal and Thermomechanical Phenomena in Electronic Systems (ITherm), 2010 12th IEEE Intersociety Conference on*, pages 1–7. IEEE, 2010.

[15] Gil Ho Yoon. Topological design of heat dissipating structure with forced convective heat transfer. *Journal of Mechanical Science and Technology*, 24(6):1225–1233, 2010.

[16] Adriano A Koga, Edson Comini C Lopes, Helcio F Villa Nova, Cícero R de Lima, and Emílio Carlos Nelli Silva. Development of heat sink device by using topology optimization. *International Journal of Heat and Mass Transfer*, 64:759–772, 2013.

[17] Tadayoshi Matsumori, Tsuguo Kondoh, Atsushi Kawamoto, and Tsuyoshi Nomura. Topology optimization for fluid-thermal interaction problems under constant input power. *Structural and Multidisciplinary Optimization*, 47(4):571–581, 2013.

[18] Joe Alexandersen, Niels Aage, Casper Schousboe Andreasen, and Ole Sigmund. Topology optimisation for natural convection problems. *International Journal for Numerical Methods in Fluids*, 76(10):699–721, 2014.

[19] Kentaro Yaji, Takayuki Yamada, Seiji Kubo, Kazuhiro Izui, and Shinji Nishiwaki. A topology optimization method for a coupled thermal–fluid problem using level set boundary expressions. *International Journal of Heat and Mass Transfer*, 81:878–888, 2015.

[20] David Makhija and Kurt Maute. Level set topology optimization of scalar transport problems. *Structural and Multidisciplinary Optimization*, 51(2):267–285, 2015.

[21] Gilles Marck, Maroun Nemer, and Jean-Luc Harion. Topology optimization of heat and mass transfer problems: laminar flow. *Numerical Heat Transfer, Part B: Fundamentals*, 63(6):508–539, 2013.

[22] EA Kontoleontos, EM Papoutsis-Kiachagias, AS Zymaris, DI Papadimitriou, and KC Giannakoglou. Adjoint-based constrained topology optimization for viscous flows, including heat transfer. *Engineering Optimization*, 45(8):941–961, 2013.

[23] Joaquim RRA Martins and John T Hwang. Review and unification of methods for computing derivatives of multidisciplinary computational models. *AIAA journal*, 51(11):2582–2599, 2013.

[24] C. Othmer. A continuous adjoint formulation for the computation of topological and surface sensitivities of ducted flows. *International Journal for Numerical Methods in Fluids*, 58(8):861–877, 2008.

[25] Yongbo Deng, Zhenyu Liu, Ping Zhang, Yongshun Liu, and Yihui Wu. Topology optimization of unsteady incompressible navier–stokes flows. *Journal of Computational Physics*, 230(17):6688–6708, 2011.

[26] Yongbo Deng, Zhenyu Liu, and Yihui Wu. Topology optimization of steady and unsteady incompressible navier–stokes flows driven by body forces. *Structural and Multidisciplinary Optimization*, 47(4):555–570, 2013.

[27] Siva Nadarajah and Antony Jameson. A comparison of the continuous and discrete adjoint approach to automatic aerodynamic optimization. *AIAA paper*, 667:2000, 2000.

[28] Michael B Giles and Niles A Pierce. An introduction to the adjoint approach to design. *Flow, turbulence and combustion*, 65(3-4):393–415, 2000.

[29] Max D Gunzburger. *Perspectives in flow control and optimization*, volume 5. Siam, 2003.

[30] Rene Pinnau and Michael Ulbrich. *Optimization with PDE constraints*, volume 23. Springer Science & Business Media, 2008.

[31] Atsushi Kawamoto, Tadayoshi Matsumori, Shintaro Yamasaki, Tsuyoshi Nomura, Tsuguo Kondoh, and Shinji Nishiwaki. Heaviside projection based topology optimization by a PDE-filtered scalar function. *Structural and Multidisciplinary Optimization*, 44(1):19–24, 2011.

[32] B. S. Lazarov and O. Sigmund. Filters in topology optimization based on Helmholtz-type differential equations. *International Journal for Numerical Methods in Engineering*, 86(6):765–781, 2011.

[33] Thomas Borrvall and Joakim Petersson. Topology optimization of fluids in stokes flow. *International Journal for Numerical Methods in Fluids*, 41(1):77–107, 2003.

[34] Khodor Khadra, Philippe Angot, Sacha Parneix, and Jean-Paul Caltagirone. Fictitious domain approach for numerical modelling of navier–stokes equations. *International journal for numerical methods in fluids*, 34(8):651–684, 2000.

[35] Casper Schousboe Andreasen, Allan Roulund Gersborg, and Ole Sigmund. Topology optimization of microfluidic mixers. *International Journal for Numerical Methods in Fluids*, 61(5):498–513, 2009.

[36] L. H. Olesen, F. Okkels, and H. Bruus. A high-level programming-language implementation of topology optimization applied to steady-state navier-stokes flow. *International Journal of Numerical Methods in Engineering*, 65:9751001, 2006.

[37] Kyungjun Lee. *Topology optimization of convective cooling system designs*. PhD thesis, The University of Michigan, 2012.

[38] William Morrow Kays and Alexander Louis London. Compact heat exchangers. 1984.

[39] Takashi Matsutani, Takanori Nakada, Yoshikazu Shinpo, and Makoto Hatano. Water jacket spacer for improvement of cylinder bore temperature distribution. Technical report, SAE Technical Paper, 2005.

[40] Jean Donea and Antonio Huerta. *Finite element methods for flow problems*. Wiley. com, 2003.

[41] F. Tröltzsch. *Optimal control of partial differential equations: theory, methods, and applications*, volume 112. Amer Mathematical Society, 2010.

[42] Jacques Louis Lions. Optimal control of systems governed by partial differential equations problèmes aux limites. 1971.

[43] Thomas Slawig. Pde-constrained control using FEMLAB–control of the Navier–Stokes equations. *Numerical Algorithms*, 42(2):107–126, 2006.

[44] Noei Petra and Georg Stadler. Model variational inverse problems governed by partial differential equations. Technical report, DTIC Document, 2011.

[45] Anders Logg, Kent-Andre Mardal, and Garth Wells. *Automated solution of differential equations by the finite element method: The FEniCS book*, volume 84. Springer Science & Business Media, 2012.

[46] K. Svanberg. The method of moving asymptotes: A new method for structural optimization. *International Journal of Numerical Methods in Engineering*, 24:359 – 373, 1987.

[47] X. Qian and O. Sigmund. Topological design of electromechanical actuators with robustness toward over-and under-etching. *Computer Methods in Applied Mechanics and Engineering*, 253:237–251, 2012.

[48] O. Sigmund and J. Petersson. Numerical instabilities in topology optimization: a survey on procedures dealing with checkerboards, mesh-dependencies and local minima. *Structural and Multidisciplinary Optimization*, 16(1):68–75, 1998.